JOURNAL OF GEOPHYSICAL RESEARCH, VOL. 106, NO. B2, PAGES 2017–2034, FEBRUARY 10, 2001

Microearthquake characteristics and crustal V_P/V_S structure at the Mid-Atlantic Ridge, 35°N

Andrew H. Barclay[1] and Douglas R. Toomey

Department of Geological Sciences, University of Oregon, Eugene, Oregon

Sean C. Solomon

Department of Terrestrial Magnetism, Carnegie Institution of Washington, Washington, D. C.

Abstract. We report on the results of a microearthquake experiment conducted at the along-axis bathymetric high of the slow spreading ridge segment near 35°N on the Mid-Atlantic Ridge (MAR). Of a total of 255 microearthquakes recorded during the 43-day experiment, 31 were located near the Oceanographer transform at the northern end of the segment, 79 occurred at the nontransform offset at the southern end of the segment, and 145 were at the segment center. At the segment center, earthquake epicenters lay within the median valley inner floor and formed a ~12-km-long trend paralleling a steep scarp bounding the western wall of the inner valley; focal depths were 3-4 km below the seafloor. Most (80%) of the focal mechanisms for 32 segment center earthquakes are consistent with normal faulting on faults approximately parallel to the axial trend. From a joint inversion for hypocenters and *P* and *S* wave velocity structures, we determined a horizontally averaged V_P/V_S ratio that decreases from 2.9 in the shallowmost 300 m to 1.7 at 2-km depth, and we interpret this decrease as indicating a decreasing contribution of thin cracks to fracture porosity with depth. The maximum depth of seismicity, 4 km, is anomalously shallow compared with other MAR segments at which microearthquake experiments have been carried out. Cross-axis relief is also anomalously low for this segment's center, and on the basis of this and other MAR microearthquake experiments, there appears to be a correlation between cross-axis relief and maximum depth of seismicity. From the correlation of cross-axis relief and inferred crustal thickness we suggest a relationship between thick crust, high crustal temperatures, and low cross-axis relief, in qualitative agreement with thermomechanical models for the depth of the axial valley.

1. Introduction

Several models have been constructed to explain the variation in axial valley relief with spreading rate [e.g., *Tapponnier and Francheteau,* 1978; *Sleep and Rosendahl,* 1979; *Phipps Morgan et al.*, 1987; *Chen and Morgan,* 1990]. A common feature of these models is that the temperature-dependent strength of the lithosphere exerts a major control on axial valley relief. However, there is considerable variation in cross-axis relief even at slow spreading ridges of comparable spreading rate. In particular, the centers of spreading segments often show reduced cross-axis relief and thicker crust [*Lin et al.,* 1990; *Shaw,* 1992; *Tolstoy et al.,* 1993; *Hooft et al.*, 2000], consistent with models in which along-axis melt delivery is focused at segment centers.

Attempts have been made to explain the along-axis variation in cross-axis relief [*Shaw,* 1992; *Shaw and Lin,* 1996] by introducing along-axis variations to models for axial valley formation. As there is little information on the thermal structure of slow spreading ridges, applying these models requires that assumptions be made for along-axis variations in temperature and crustal rheology. Reduced cross-axis relief is attributed to higher crustal temperature at a given depth, but there is no direct observational evidence for a correlation between axial morphology and crustal thermal structure. Because the thickness of the seismogenic layer may be influenced by the crustal temperature structure, the cross-axis relief should increase as a function of maximum depth of seismicity, for a given spreading rate.

This relationship may be explored by comparison of the maximum earthquake focal depths between segments with different cross-axis relief. However, previous microearthquake studies along the Mid-Atlantic Ridge (MAR) have yielded results for the maximum depth of seismicity only in regions of large cross-axis relief: at segment ends [*Toomey et al.,* 1988; *Wolfe et al.,* 1995] and at the centers of ridge segments that display inner valley relief in excess of 800 m and lack features indicative of a high magmatic flux [*Kong et al.,* 1992; *Wolfe et al.,* 1995]. All of these studies yielded a maximum depth of seismicity of 5.5-8 km below the seafloor, and given the uncertainties in the measurement of focal depth (~1 km), no correlation between maximum focal depth and cross-axis relief could be identified. The maximum focal

[1]Now at Department of Geology and Geophysics, Woods Hole Oceanographic Institution, Woods Hole, Massachusetts.

Paper number 2000JB900371.
0148-0227/01/2000JB900371$09.00

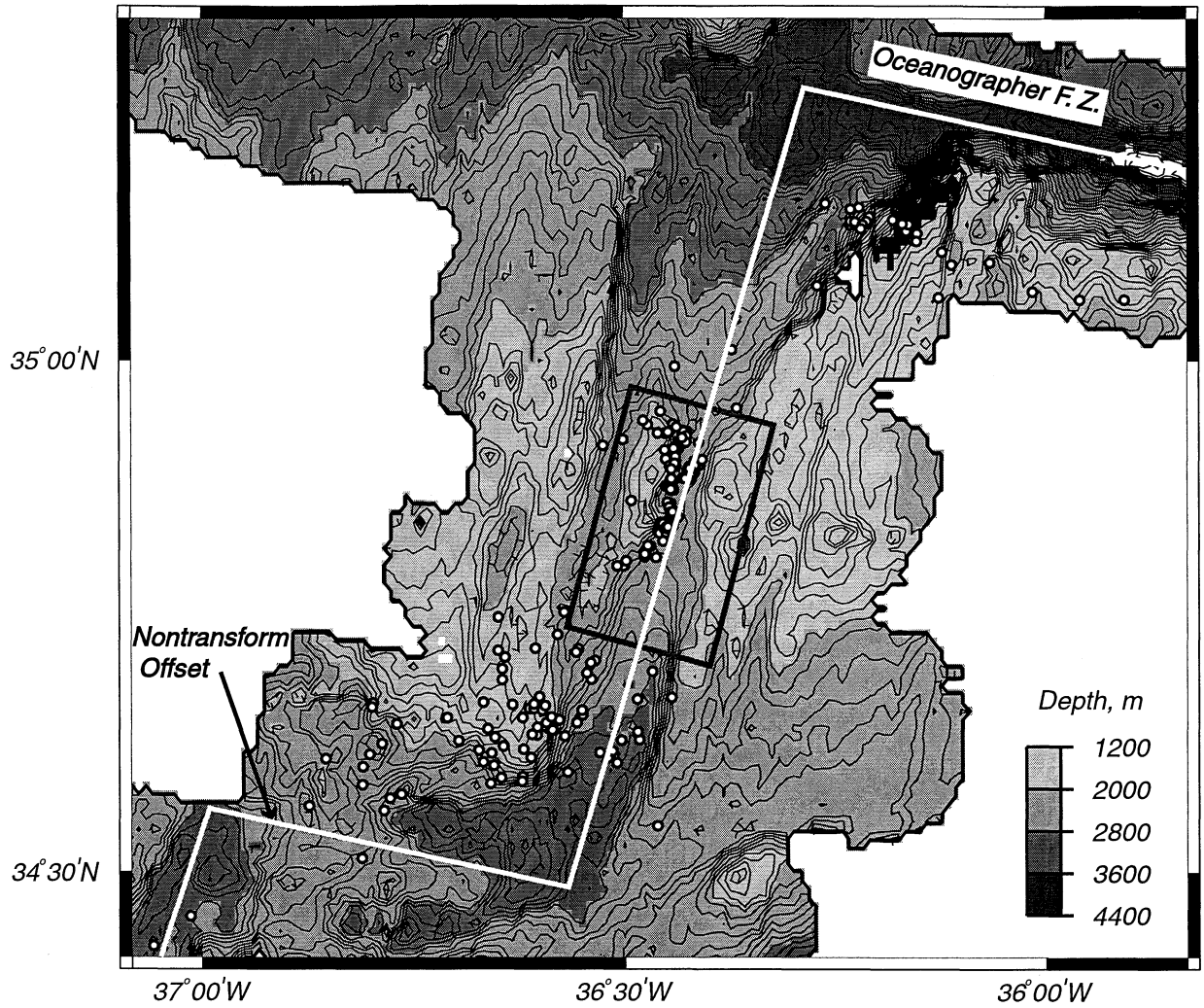

Figure 1. Multibeam bathymetry of the Mid-Atlantic Ridge segment at 35°N. Circles denote earthquake epicenters relocated using HYPOINVERSE, a one-dimensional velocity structure, and a constant VP/VS ratio of 1.9. The box at the segment center encompasses the ocean bottom seismometer (OBS) locations and delimits the area of Figures 4, 7, 8, 10, and 13. Contour interval is 200 m, and shading changes every 800 m. The white line indicates the approximate position of the plate boundary.

depth at a segment that shows evidence for anomalously high crustal temperatures and cross-axis relief of significantly less than 800 m (the lowest cross-axis relief at which focal depths have been determined [*Wolfe et al.,* 1995]) is required in order to test for this correlation.

The center of the MAR ridge segment near 35°N is known to be a region of enhanced crustal magmatism. This segment is located between the Oceanographer Fracture Zone to the north and a nontransform offset to the south (Figure 1) and has a length of 90 km, making it one of the longest segments of the MAR. Seismic refraction [*Hooft et al.,* 2000] and mantle Bouguer anomaly [*Detrick et al.,* 1995] data indicate pronounced along-axis variations in crustal thickness, from 4 km at the segment ends to >8 km at the segment center. A chain of seamounts near the segment center provides further evidence for enhanced magmatism [*Bideau et al.,* 1996]. One of these seamounts is underlain by a shallow low-velocity body at 1-2-km depth, interpreted by *Barclay et al.* [1998] as a region of near-solidus temperatures. Low P wave velocities have also been detected at depths >3.5 km beneath the segment center and have been interpreted as regions of high temperatures and possibly partial melt [*Magde et al.,* 2000]. In addition, the cross-axis relief from the inner valley floor to the first crest of the valley walls at the segment center is anomalously low, only ~300 m. All of these attributes are consistent with a melt supply from the mantle that is focused toward the segment center, resulting in higher than normal crustal temperatures there.

In 1992 we carried out a joint active- and passive-source seismic experiment within the inner valley floor of the MAR near 35°N. The primary aim of this experiment was to characterize the depth distribution of seismicity beneath the center of a segment with low cross-axis relief and to compare it with results obtained elsewhere. Results of the active-source portion of the experiment were presented by *Barclay et al.* [1998]. In this paper we characterize the microearthquake seismicity of the 35°N segment and use the available P and S wave delay times to image the structures of P and S wave

velocity, V_P and V_S, respectively. From the hypocentral locations and focal mechanisms we demonstrate that earthquakes near the segment center extend only to 4-km depth and are primarily the result of normal faulting at the base of faults that bound the median valley inner floor. On the basis of a comparison of the maximum depth of seismicity, cross-axis relief, and crustal thickness for four MAR segments, we demonstrate that along-axis variations in relief are coupled to variations in thermal structure and crustal thickness, in general agreement with current models.

2. Microearthquake Experiment

We deployed 14 ocean bottom seismometers (OBSs) on and around the inner floor of the axial valley (Figure 1). The OBS network, which had an approximate spacing between instruments of 4 km, covered an area of ~18 by 10 km^2 and was situated near and to the south of the along-axis bathymetric high defining the segment center. Each OBS included three orthogonal 1-Hz seismometers and a hydrophone. Details of the instrumentation, clock corrections, and instrument relocation were given by *Barclay et al.* [1998]. The OBSs were programmed to record for 40 s whenever the energy on the trigger channel, averaged over a 3-s time window, exceeded the energy averaged over a 10-s window by a factor F. The OBSs triggered on the hydrophone channel for 33 days, with $F = 3$, and then on the vertical channel for the remaining 10 days of the deployment with $F = 7$. During the 43-day-long experiment, 13 seismometers recorded an average of 1870 triggered events, and one seismometer failed to record. The seismometers also recorded P wave arrivals from 1831 airgun shots; a tomographic inversion of these travel times for P wave velocity structure was described by *Barclay et al.* [1998]. Travel times from 1431 of these shots were combined with the earthquake arrival times in a joint inversion described in this paper.

We identified potentially locatable events by manually inspecting arrivals that triggered on four or more OBSs within a 10-s period. Of these 496 events, 255 were earthquakes, while the remainder included whale songs, microseism activity, multiple triggers on the codas of large earthquakes, and unidentified sources. The seismograms fell into two classes: those with clear, impulsive P and S wave arrivals, multiple water column bounces, and P-S arrival time differences of ~1 s (Figure 2) and those with more emergent arrivals, longer codas, and P-S time differences of 3-5 s. No teleseismic arrivals triggered on any of the OBSs.

P and S wave arrival times were picked using an automatic predictive-filtering technique [*Takanami and Kitagawa,* 1988], which was calibrated, verified, and supplemented by manual picking. P wave arrivals were preferentially picked on the vertical seismometer channel; otherwise the hydrophone channel was used. The S wave arrivals showed evidence of splitting with a time delay between the fast and slow arrivals of ~100 ms. We picked the earlier arrival after rotating each horizontal seismogram pair into axis-parallel (fast) and axis-perpendicular (slow) orientations. This rotation was motivated by polarization analysis of the S wave arrivals [*Barclay et al.,* 1995] and by observations of P wave azimuthal anisotropy from the coincident active-source tomography experiment [*Barclay et al.,* 1998], both of which

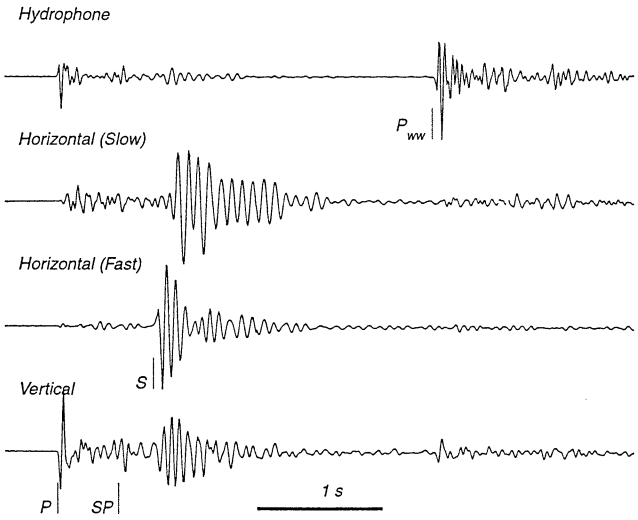

Figure 2. Example seismograms of an impulsive arrival from a segment center earthquake recorded on the four components of a single OBS. P wave and split S wave arrivals (denoted by vertical lines) are followed by the first water column reverberation P_{ww}. The arrival labeled SP is attributed to an S-to-P conversion at the interface between seismic layers 2A and 2B. The horizontal components have been rotated into axis-parallel (fast) and axis-perpendicular (slow) directions. The reverberatory nature of the S arrival is likely due to poor coupling and seismometer resonance. Each seismogram has been normalized to the largest amplitude within the time window shown.

are consistent with a predominantly axis-parallel orientation of vertical cracks. An arrival time uncertainty was assigned to each pick; these ranged from 8 to 48 ms for the P waves and from 10 to 100 ms for the S wave arrivals.

3. Hypocentral Location

We used three different methods to locate the hypocenters in order to exploit the advantages of each. We began with a linearized inversion method (HYPOINVERSE [*Klein,* 1978]) to locate all 255 microearthquakes, including those distant from the OBS network. In order to include bathymetry explicitly, to explore the effects of varying the V_P/V_S ratio, and to determine proper 95% confidence regions we next used a grid search method. Computation limits restricted our grid search analysis to the events closest to the OBS network, at the segment center. Finally, we used a joint linearized inversion approach to invert simultaneously for the hypocenters of the best recorded earthquakes and for one- and three-dimensional P and S wave velocity structures.

3.1. All Hypocenters: HYPOINVERSE

The HYPOINVERSE method [*Klein,* 1978] uses a linearized inversion with step length damping to determine the four hypocentral parameters (coordinates x, y, z, and origin time, where x and y are the abscissa and ordinate of the bold box in Figure 1 and z is depth) for each event, given a one-dimensional velocity structure and a constant V_P/V_S ratio. A station correction can be applied to the arrival times at each receiver to account for variations in receiver depths and near-receiver velocity structure. For the P wave velocity structure

we averaged the structure along a 40-km length of the inner valley from a two-dimensional refraction experiment [*Hooft et al.*, 2000]. We chose a constant V_P/V_S ratio of 1.9 on the basis of the grid search results discussed below, although we also explored the effects of V_P/V_S values ranging from 1.7 to 2.0. Initial station corrections were calculated relative to a datum of 2250 m below sea level, assuming a constant velocity of 6.5 km/s. The correction at each station was then iteratively adjusted by the mean travel time residual after location of the well-recorded segment center earthquakes. A starting focal depth of 5 km was used for all microearthquakes.

The epicenters determined using HYPOINVERSE fall into three groups, which encompass the entire segment (Figure 1). The largest group of events, 145 in number, was situated at the segment center. Another cluster of 79 epicenters was located at the southern end of the segment, while the smallest group of 31 events was situated in or near the Oceanographer Fracture Zone to the north of the segment. Events in the latter two groups lay well outside the seismometer network; because their focal depths were poorly constrained, they were located using a fixed focal depth of 5 km. The areas of 95% confidence (assuming that the velocity structure and V_P/V_S ratio are known) for the segment end epicenters were 3-7 km in diameter. All of the epicenters were situated within 20 km of the plate boundary.

The northern group of microearthquakes appear to be associated with the Oceanographer Fracture Zone. They form a trend approximately parallel to that of the transform fault valley, but as shown in Figure 1, the seismicity falls south of the fracture zone by ~12 km. The latitude of this trend, however, depends strongly on the V_P/V_S ratio; decreasing the V_P/V_S ratio to 1.7 places these earthquakes within the transform and improves their alignment with the fracture zone. Assuming that the events lie within the transform boundary, we infer that the average V_P/V_S ratio along ray paths between the segment center and the northern group of events is lower than the value of 1.9 measured at the segment center from the grid search (see below). Most of the earthquakes in this northern group are located near the intersection of the axial valley and fracture zone or within the inside corner.

At the southern end of the segment the epicenters are concentrated around the inside corner high. Here the epicentral distribution shifts much less as V_P/V_S is changed. High levels of microearthquake activity at a Mid-Atlantic Ridge inside corner of a nontransform offset have also been reported by *Wolfe et al.* [1995]. A small number (~20) of earthquakes lie beneath the inner valley floor at the segment end near longitude 36°30'W. Another group of 13 epicenters appears to be associated with an axis-parallel ridge that bisects the nontransform offset near longitude 36°50'W. Decreasing the V_P/V_S ratio to 1.7 relocated these earthquakes directly below this morphologic feature. With the exception of these events, no epicenters lie within the deepest portions of the nontransform offset.

The third, and largest, group of seismicity was concentrated beneath the inner valley of the segment, straddling the along-axis high at the segment center. Most of these earthquakes (139 out of 145) were located directly below or within one station spacing (4 km) of the OBS network, giving a high likelihood for good resolution of hypocentral parameters, focal mechanisms, and moment magnitudes. The remainder of this paper will concentrate on these events. The absence of microearthquakes within the inner valley floor between the central and southern groups during our experiment is real. The seismometer network extended across this region, and its sensitivity to earthquakes here was as high as at the segment center.

3.2 Segment Center Earthquakes: Grid Search

We used a grid search method to relocate the segment center seismicity. Our method was based on that of *Rowlett and Forsyth* [1984], and we evaluated 95% confidence regions using the approach of *Wilcock and Toomey* [1991], as corrected by *Sohn et al.* [1998]. A shortest-path ray-tracing method [*Moser*, 1991] was used to determine travel times to every receiver from every node on a 0.25-km three-dimensional grid. Bathymetry was included by shearing columns of nodes in accordance with the seafloor relief. We used the same one-dimensional velocity structure as for the HYPOINVERSE locations, and we relocated using a range of

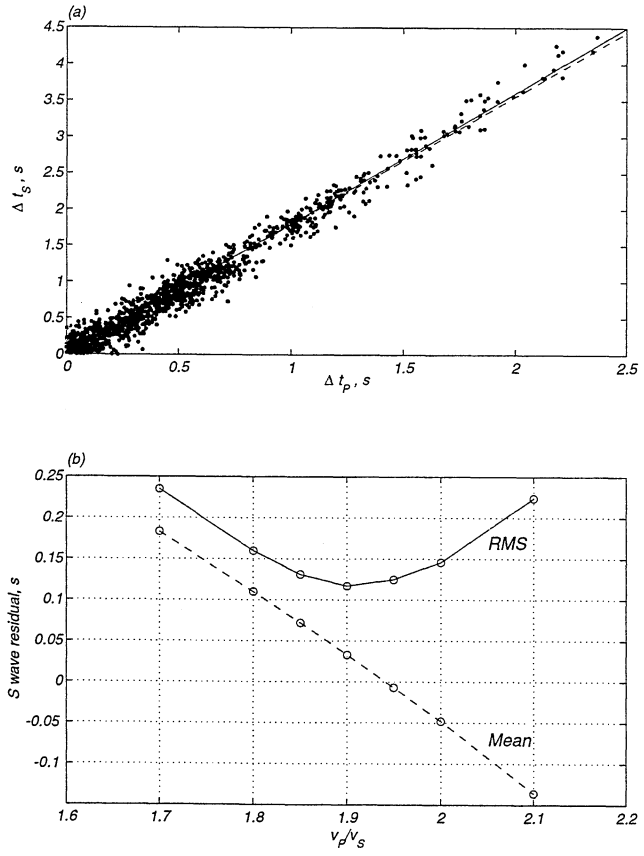

Figure 3. Determination of V_P/V_S. (a) Differential arrival times. Each point represents the S wave arrival time difference Δt_S between a pair of receivers for a single earthquake plotted against the P wave arrival time difference Δt_P for the same receivers and events. The solid line corresponds to the best fitting V_P/V_S ratio of 1.8. (b) S wave arrival time residuals for the segment center earthquakes following grid search relocation plotted as a function of V_P/V_S ratio. The solid line indicates the RMS residual for arrival times, and the dashed line shows the mean arrival time residual. The RMS residual is a minimum at V_P/V_S=1.9, and the mean residual is zero at V_P/V_S=1.94.

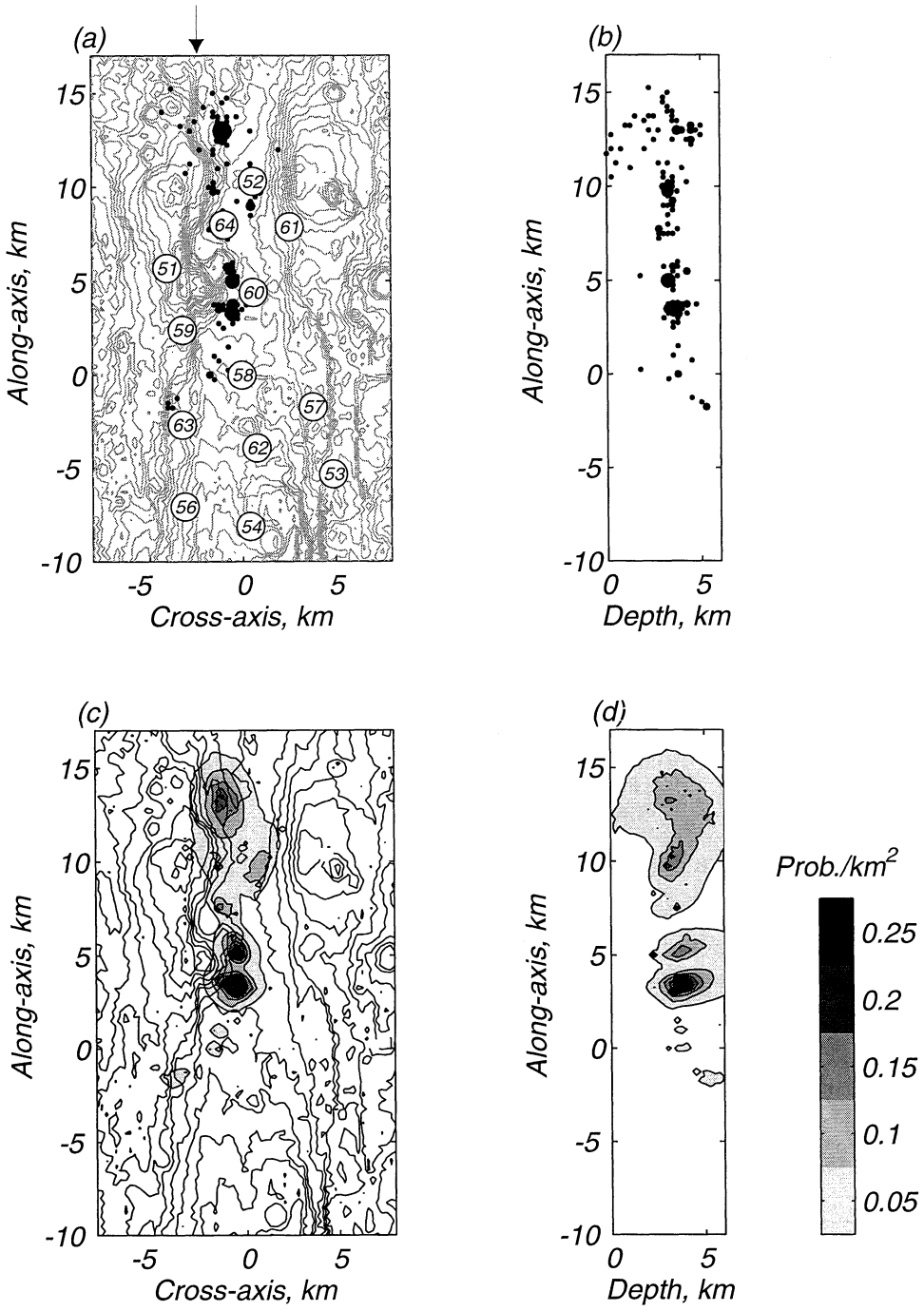

Figure 4. Results of grid search hypocentral relocation for 139 segment center microearthquakes. (a) Epicenters superimposed on bathymetry. The contour interval is 50 m. Open circles and numbers denote OBS positions and names. The arrow shows the approximate position of the western valley-bounding scarp. (b) Cross section of hypocenters along axis. The radius of each circle is proportional to the number of earthquakes relocated at each grid point. (c and d) Empirical hypocentral probability density for the same earthquakes, plotted on the same scales as Figures 4a and 4b, respectively. Bathymetric contour interval in Figure 4c is 100 m. The areas of Figures 4a and 4c coincide with the box in Figure 1.

depth-independent V_P/V_S ratios from 1.7 to 2.0. Arrival times were weighted inversely to the squares of the estimated picking uncertainties.

A major source of uncertainty in the hypocentral relocation was the V_P/V_S ratio. We attempted to apply the method of *Francis* [1976] in order to estimate the V_P/V_S ratio, but this approach gave highly variable estimates ranging from 1.6 to 2.0 (Figure 3). The weighted root-mean-squared (RMS) error between the points in Figure 3 and the straight line that corresponds to the best fitting V_P/V_S ratio of 1.8 is 75 ms, a figure larger than the RMS error of 40 ms we would expect if the only source of error was picking uncertainty. Since the

main assumption of the *Francis* [1976] method is a constant V_P/V_S, the most likely reason for the scatter is variable V_P/V_S structure below the seismometer network, as discussed in section 3.3. We instead estimated the best fitting value of V_P/V_S by testing a range of constant V_P/V_S values in the grid search and finding the value which minimized both the *S* wave RMS residual and the mean *S* wave residual. The RMS and mean residuals were minimized at V_P/V_S values of 1.9 and 1.94, respectively (Figure 3b); we chose a constant V_P/V_S ratio of 1.9, which gave RMS arrival time residuals of 41 and 117 ms for *P* and *S* waves, respectively.

The results of the grid search relocation for 139 segment center events are shown in Figure 4. Figures 4a and 4b show the best fitting hypocenters, while Figures 4c and 4d show the empirical hypocentral probability density. This quantity represents the a posteriori probability of a hypocenter occurring within a given area during the 43-day duration of the microearthquake experiment. It is the sum of the normalized hypocentral probability densities for all of the relocated earthquakes, projected to the *x-y* and *z-y* planes in Figures 4c and 4d, respectively (where *x* and *y* are the abscissa and ordinate of Figures 4a and 4c, respectively, and *z* is depth). It incorporates the number of earthquakes as well as their hypocentral uncertainties. A volume integral of this density function is equal to the total number of relocated hypocenters.

Most of the epicenters lie within a 12-km length of the inner valley floor. With the exception of a group near $x = 1$, $y = 10$ the epicenters lie along an axis-parallel trend that is located 2-3 km east of a steep scarp (~300 m high) that defines the western wall of the inner valley. In addition, the along-axis extent of the seismicity (between $y = -2$ and $y = 16$) and the scarp are comparable. More than half of the epicenters are located within three clusters, at $x = -1$ and y = 3, 5, and 13 km; these clusters are most evident in Figure 4c. The southernmost two clusters are located to the east of a near-axis volcano, which is underlain by a *P* wave low-velocity volume [*Barclay et al.,* 1998]. The 2 σ confidence regions for individual epicenters are mostly <1 km, increasing toward the north as the hypocenters become more distant from the OBS network.

The earthquakes are consistently located at 3-4 km depth below the seafloor and show no significant along-axis variation in the maximum focal depth. For the events directly below the network the 2 σ uncertainty in focal depth is ~1.5 km. Some of the northern hypocenters are shallower, but because these earthquakes were distant from the OBS array, their depths are less well constrained, and it is possible that these earthquakes also have focal depths of 3-4 km.

Vector differences between the grid search and HYPOINVERSE locations for the segment center hypocenters are generally <500 m. We attribute these differences to the station corrections (which are empirical but may account for some velocity heterogeneity that the grid search method, which uses a one-dimensional velocity structure, cannot), the explicit inclusion of bathymetry in the grid search method, differences in the ray-tracing methods, and the requirement imposed by the grid search method that hypocenters lie at one of the grid nodes. Notably, neither method reduced the RMS travel time residuals to levels comparable to the data uncertainty since the *P* and *S* wave RMS residuals were significantly greater than the respective estimated residuals of 11 and 35 ms (approximated by the weighted RMS value of the arrival time picking uncertainties).

3.3. Joint Inversion for Segment Center Hypocenters, V_P, and V_S

As the arrival time data are not well modeled by hypocenter adjustments alone, we developed a joint inversion method to solve for three-dimensional *P* and *S* wave velocity structures as well as hypocentral parameters. We based our approach on the tomographic inversion method of *Toomey et al.* [1994], which uses shortest-path ray tracing. We linearize the problem as

$$\mathbf{Gm} = \mathbf{d}, \tag{1}$$

where **m** is a vector of model parameters comprised of *P* and *S* wave slowness perturbations and hypocentral perturbations relative to a starting model and **d** contains the *P* and *S* wave arrival time residuals relative to those predicted by the starting model. The vector **d** includes both residuals for the earthquake arrivals and the *P* wave travel time residuals for shots. Here **d** and **m** are related by the sparse partial derivative matrix **G**. Each row of (1) may be expressed as

$$\delta T = \int_R \left(\frac{\partial t}{\partial u} \delta u \right) ds + \sum_{i=1}^{3} \frac{\partial t}{\partial x_i} \delta x_i + \delta T_o , \tag{2}$$

where δT is a *P* wave travel time residual or a *P* or *S* wave arrival time residual, T_o is the origin time, **x** is the hypocentral location, *s* is the arc length, and *t* is the travel time calculated along path *R* through a slowness structure defined by $u(\mathbf{r})$, where **r** is a position vector. The calculation of the slowness partial derivatives is described by *Toomey et al.* [1994]. The hypocentral partial derivatives were determined from the gradient of the travel time field, which was calculated for each OBS using the shortest-path ray tracer. For the airgun data the second and third terms on the right-hand side of (2) are zero. In our formulation, **m** contains δu, δx_i, and δT_o and is a vector of length $(4N + p + q)$, where *N* is the number of earthquakes and *p* and *q* are the number of perturbational nodes for the *P* and *S* wave slowness structures, respectively. Here **d** contains δT, and its length is equal to the total number of observations (earthquake *P* and *S* wave arrival times and airgun *P* wave travel times).

We regularized the inversion by adding smoothing, damping, and coupling constraints to (1). Vertical and horizontal smoothing was applied to the *P* and *S* wave slowness models, and damping was applied to the hypocentral perturbations. The implementation of smoothing and damping constraints was similar to that described by *Toomey et al.* [1994]. An additional coupling constraint was applied to the *P* and *S* wave slowness models by minimizing, for each node, the expression $\delta u_S - \delta u_P \, \mu(z) = 0$, where $\mu(z)$ is a depth-dependent V_P/V_S ratio. This constraint was applied for two reasons: to stabilize the inversion for V_S and to derive an estimate for V_P/V_S versus depth that is minimally compromised by the more poorly resolved *S* wave structure [*Michelini,* 1993].

The regularized inversion can be expressed as the minimization of

$$s^2 = \mathbf{d}\mathbf{C}_d^{-1}\mathbf{d}^{\mathbf{T}} + \sum_{i=1}^{6} \lambda_i \mathbf{m}\mathbf{C}_i^{-1}\mathbf{m}^{\mathbf{T}}, \quad (3)$$

where $\mathbf{C}_d$ is the data covariance matrix, $\mathbf{C}_1$ and $\mathbf{C}_2$ are the horizontal and vertical smoothing constraints on the P wave velocity structure, $\mathbf{C}_3$ and $\mathbf{C}_4$ are the corresponding constraints on the S wave velocity structure, $\mathbf{C}_5$ represents damping on the hypocentral parameters, and $\mathbf{C}_6$ is the V_P/V_S constraint, as defined above. The λ_i are multipliers that are varied to change the relative importance of the constraints.

Convergence to the best fitting model required several iterations of ray tracing and solution of (1) in order to allow for nonlinear effects (i.e., changing ray paths and hypocentral partial derivatives). We used the same starting P wave velocity structure as for the grid search and HYPOINVERSE locations. The starting values for the hypocenters were taken from the output of the grid search location (Figure 4). Only the best constrained earthquakes (those with epicenters inside or within one station spacing, 4 km, of the OBS network) were included, which reduced the number of microearthquakes from the 139 used in the grid search to 91 and gave a total of 560 P wave and 400 S wave arrival times. Travel times from 1431 airgun shots [*Barclay et al.,* 1998] were included in order to constrain the P wave velocity structure in the uppermost ~2.5 km of the crust.

3.3.1. Constraints on V_P/V_S in seismic layer 2A. We determined the mean value of V_P/V_S in seismic layer 2A from the relative arrival times of direct S wave and converted P wave phases, and we used the result to constrain the P and S wave velocity structures during the joint inversion. Our measurement of the average V_P/V_S in the shallowmost crust was based on the identification of a P wave arrival (denoted by *SP* in Figure 2) observed on most seismograms and at all instruments. This phase arrived between the direct P and S waves, was more prominent on the vertical seismometer and hydrophone than on the horizontal seismometers, and had an amplitude that often exceeded that of the direct P wave. In addition, the arrival preceded the direct S wave by a similar time (300-400 ms) for all source-receiver pairs, whereas the delay between the arrival and the direct P wave was more variable (0.5-1.5 s), as shown in Figure 5. From these observations we infer that the arrival is a P wave that was converted from the direct S wave at a near-receiver interface. The constant time delay between the arrival and the direct S wave across the OBS network suggests that the converting interface is present at a similar depth within the area of the experiment. The conversion likely occurred at the large velocity gradient associated with the transition from seismic layer 2A to layer 2B. Converted P wave arrivals, attributed to the 2A/2B transition, have been observed in active-source experiments at other mid-ocean ridges [e.g., *Christeson et al.,* 1997; *Collier and Singh,* 1998]. At 35°N a sharp increase in the depth-dependent P wave velocity (from 3.5 km/s at 300 m to 5 km/s at 400 m depth) has been measured beneath the

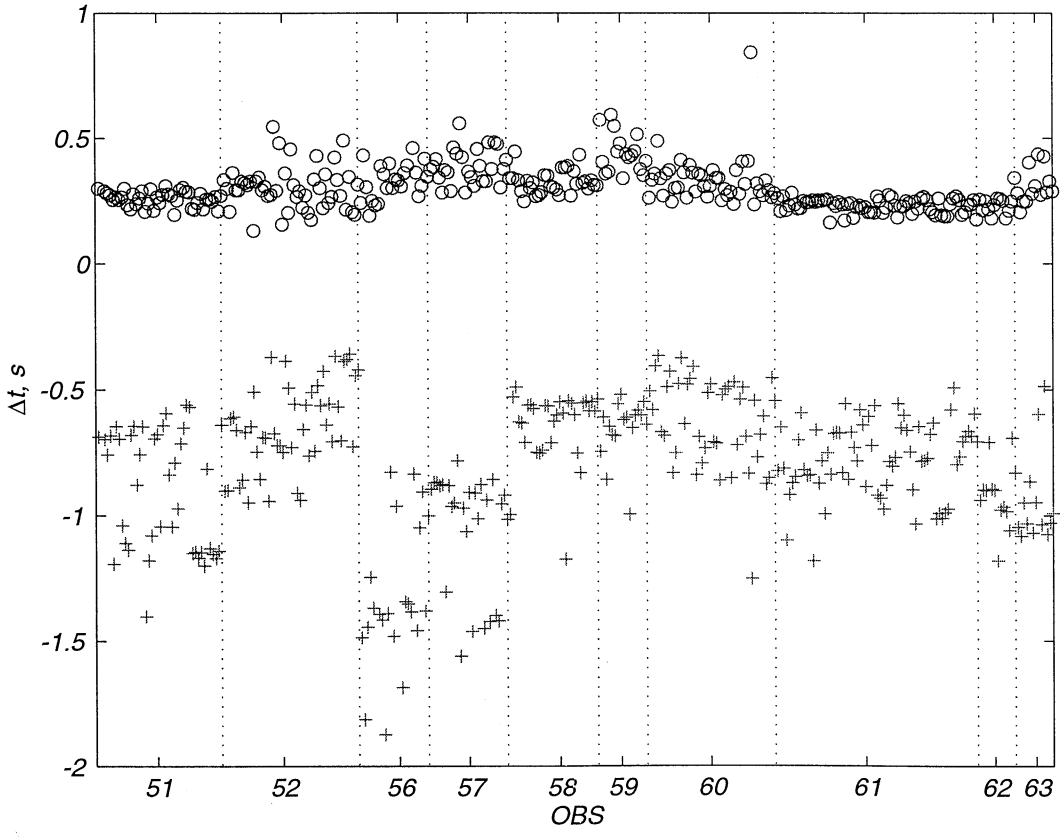

Figure 5. Arrival times of the direct P and S waves, plotted relative to the arrival times of the converted phase, for 375 seismograms at 35°N. The direct P waves (arrival times denoted by crosses) are followed by the converted P waves (at $\Delta t = 0$) and then the direct S waves (circles). Dotted lines separate observations from different receivers (identified in Figure 4a). The mean arrival time difference between the direct S wave and converted P wave is 314 ms, with a standard deviation of 70 ms.

inner valley floor and has been interpreted as the layer 2A/2B transition [*Hussenoeder,* 1998]. The seismic reflection associated with this gradient has a constant two-way travel time along at least an 8 km length of the inner valley floor [*Hussenoeder,* 1998], suggesting that a sharp layer 2A/2B boundary is ubiquitous and at a nearly constant depth beneath the inner valley at 35°N.

We calculated the mean V_P/V_S ratio in the shallowmost 300 m, under the assumption that the conversion occurred at the base of layer 2A. The average V_P/V_S ratio along a ray path is equal to $(t_P + \delta_{SP}) / t_P$, where t_P and $(t_P + \delta_{SP})$ represent the P and S wave travel times, respectively, and δ_{SP} is the difference between the P and S wave arrival times. By calculating t_P for a vertically propagating P wave through layer 2A using the velocity profile of *Hussenoeder* [1998] and by averaging the observed arrival time differences between the converted P and direct S arrivals to give δ_{SP}, we determined a V_P/V_S value of 2.9±0.4. Although this value is large compared to the mean value in the oceanic crust of 1.8, it is in agreement with other determinations of V_P/V_S in the shallowmost oceanic crust [e.g., *Spudich and Orcutt,* 1980; *Collier and Singh,* 1998].

3.3.2. Joint inversion for one-dimensional structure. We first inverted for one-dimensional (depth-dependent) P and S wave velocity structures. The best fitting P and S wave velocity models are shown in Figure 6. The starting S wave structure was derived from the starting P wave structure used in the grid search by adopting a V_P/V_S value of 1.9, except at the two shallowmost perturbation nodes (0 and 250 m depth) where the V_P/V_S value was fixed at 2.9. The RMS residuals for the resulting model (Figure 6) were 45, 47, and 85 ms for the shots, earthquake P, and earthquake S times, respectively. In addition to the high value of V_P/V_S imposed in the shallow crust, the models show monotonic increases in V_P and V_S with increasing depth and a decrease in V_P/V_S to 2 km depth. At greater depth, V_P/V_S increases as V_S decreases and V_P remains approximately constant. The decrease in V_P/V_S down

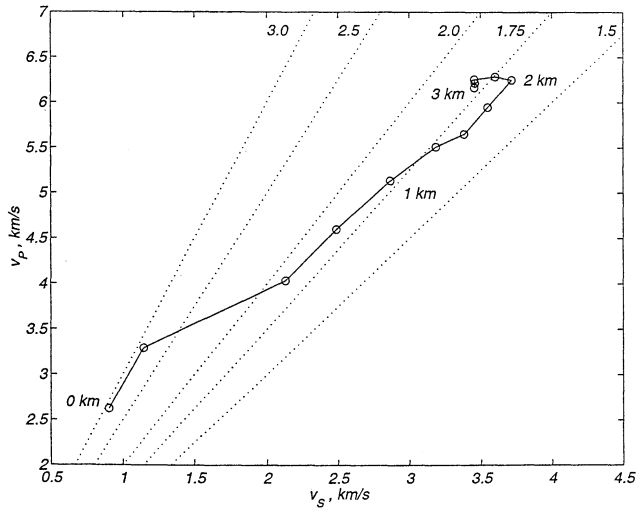

Figure 6. Best fitting one-dimensional (depth-dependent) P and S wave velocity structures. The solid line is the joint velocity model; circles represent depth nodes every 250 m, and linear interpolation is assumed between nodal values. Lines of constant V_P/V_S at 1.5, 1.75, 2.0, 2.5, and 3 are dotted.

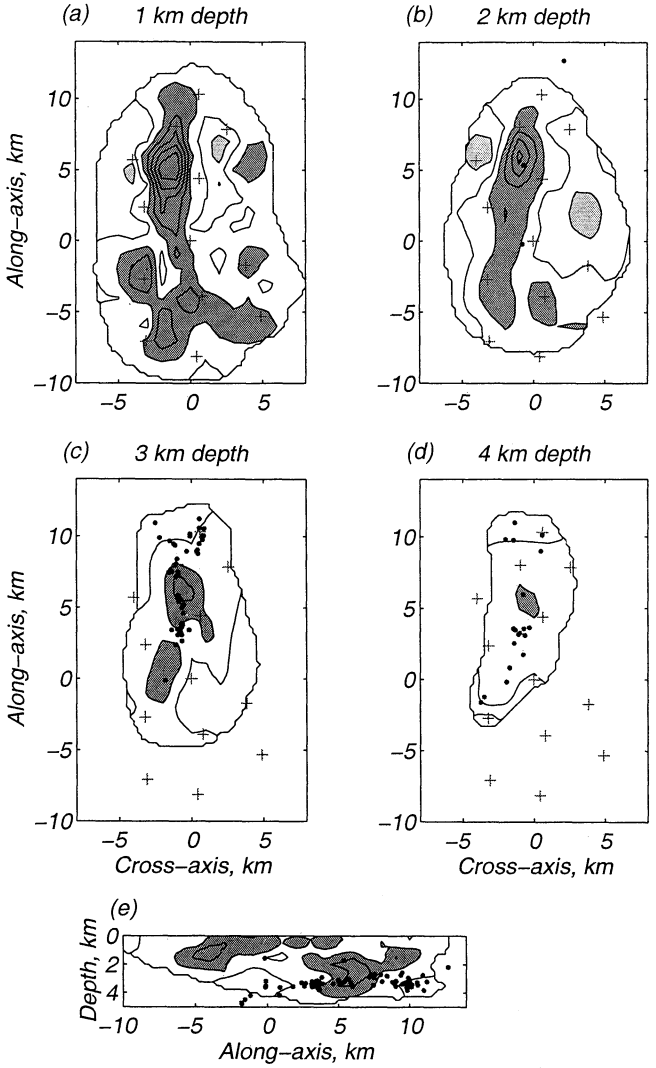

Figure 7. Best fitting P wave velocity model from joint inversion. (a-d) Horizontal slices through the tomographic image, contoured at 0.2 km/s intervals relative to the starting velocity structure for depths beneath the seafloor of 1, 2, 3, and 4 km, respectively. Crosses denote OBS locations; solid circles are hypocenters projected onto the nearest depth slice. (e) Along-axis vertical section through the tomographic image at x = 0 km. Solid circles are hypocenters projected onto the plane of the section. Perturbations >0.2 and less than -0.2 km/s are shaded light and dark, respectively; the images have been masked in regions of low ray coverage. The coordinate system of Figure 4 is used.

to 2-km depth appears to be a stable feature; resolution tests indicate that such a decrease can be resolved and that it is a consistent feature of a large range of models, including those with unconstrained V_P/V_S. The increase in V_P/V_S at depths greater than 2 km is not well resolved, however, and as this increase is mainly due to a sharp decrease in V_S, we attribute it to poor resolution. Low V_P/V_S values of 1.7 at ~1.5 km depth below basement have been observed in oceanic crust at other locations [*Spudich and Orcutt,* 1980; *Au and Clowes,* 1984; *Christeson et al.,* 1997].

3.3.3. Joint inversion for three-dimensional structure. After joint inversion for hypocenters and depth-dependent

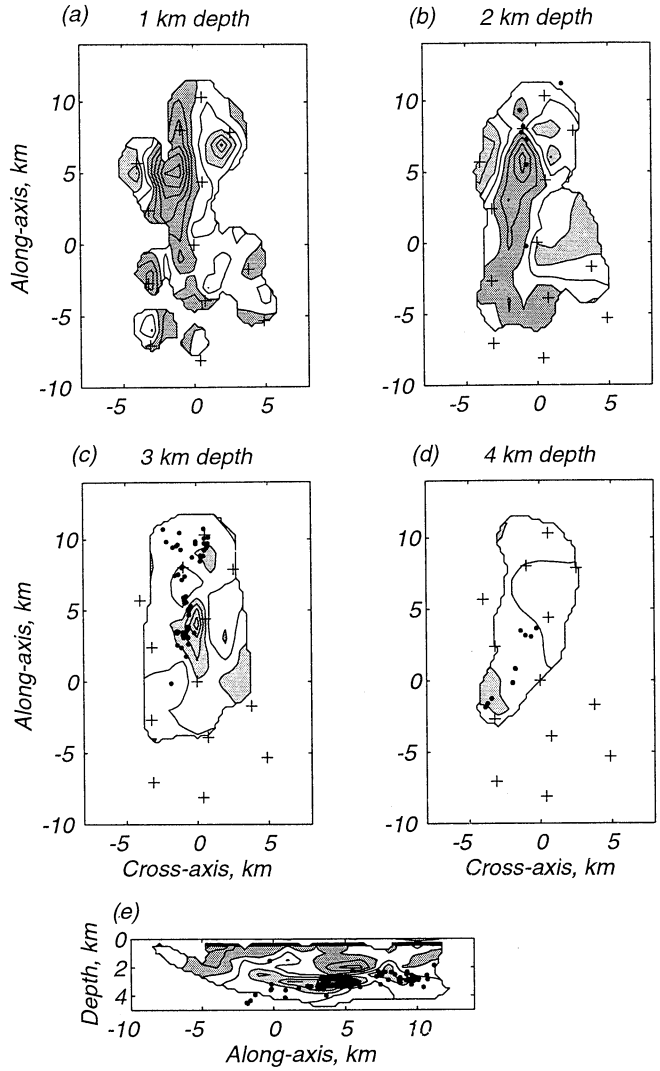

Figure 8. Best fitting S wave velocity model from joint inversion. (a-d) Horizontal slices through the tomographic image, contoured at 0.2 km/s intervals relative to the starting S wave velocity structure for depths beneath the seafloor of 1, 2, 3, and 4 km, respectively. Crosses denote OBS locations; solid circles are hypocenters projected onto the nearest depth slice. (e) Along-axis vertical section through the tomographic image at x = 0 km. Solid circles are hypocenters projected onto the plane of the section. Perturbations >0.2 and less than -0.2 km/s are shaded light and dark, respectively; the images have been masked in regions of low ray coverage. The coordinate system of Figure 4 is used.

velocity structures, the RMS misfits were still greater than the expected values. We therefore inverted for hypocenters and three-dimensional P and S wave velocity structures, using the same depth-dependent starting velocity models and V_P/V_S constraints as were used for the one-dimensional inversion. The misfits for the best fitting model were 18, 28, and 46 ms for the shot, earthquake P, and earthquake S data, respectively, and represent a significant improvement over the one-dimensional solution.

Sections through the three-dimensional P wave velocity structure are shown in Figure 7. The sections in Figure 7 only show regions which were sampled by the rays and are masked for regions in which the normalized derivative weight sum (DWS; see *Toomey et al.* [1994]) was <1. The uppermost 2.5 km of the velocity structure is primarily constrained by the airgun data and is similar to the structure described by *Barclay et al.* [1998]. The most prominent feature in the uppermost 2 km is a region of low seismic velocities, centered at x = -2, y = 5. This feature is located directly beneath a near-axis seamount and was interpreted by *Barclay et al.* [1998] as a region of high temperatures and/or partial melt. The addition of the earthquake data further constrains the velocity structure down to ~4 km depth and shows that the shallow, low-velocity region at x = -2, y = 5 becomes a ~3-km-wide, axis-parallel band of low seismic velocities (with a maximum amplitude in excess of -0.2 km/s) beneath the western half of the inner valley.

Results of the inversion for S wave structure are shown in Figure 8. At a given depth, lateral variations in the S wave structure are large (~1 km/s at 2 km depth) and vary on a scale of 2-5 km. Many of these variations are constrained only by near-vertical ray paths to single receivers, and their resolution is therefore poor. Similarly, the high shear wave velocity feature surrounding the hypocenters at 3-4 km depth in Figure 8e is likely an artifact due to poor ray sampling in the source region. However, a cross-axis asymmetry of longer wavelength is apparent at depths shallower than 3 km, with lower velocities beneath the western half of the inner valley compared with the eastern half. As this asymmetry is constrained by many receivers, it is likely to be real. In addition, the western low velocities may be correlated with the axis-parallel band of low velocities in the P wave tomographic image (Figure 7). The low S wave velocities are not caused by coupling with the P wave structure since they are also present in inversions with no V_P/V_S constraints.

Resolution tests indicate that the amplitudes of the three-dimensional perturbations in S wave velocity structure are poorly resolved, especially when compared with the resolution of the P wave structure, whereas the spatial distribution of large anomalies (horizontal dimensions of ~4 km or more) is recoverable. We created a synthetic S wave velocity structure by reducing the S wave starting velocity structure by 0.4 km/s (~10%) in a checkerboard pattern of blocks which were each 4 km in lateral dimension and 1.5 km in depth (Figure 9). Arrival times were calculated for this structure using the same hypocenters, OBS locations, and pick uncertainties as for the data inversion. Random noise was added to the arrival times, the starting hypocenters were randomly perturbed by <500 m in all three directions, and the P wave velocity structure was unperturbed from the starting structure. The synthetic arrival times were then inverted using the same parameters and constraints as those used for the data inversion. The results (Figure 9) show that the checkerboard pattern is not well recovered except beneath the inner valley and above the hypocenters. The region of moderate recovery compares well with the unmasked region in Figure 8. The resolution tests indicate that the resolution is poor a few kilometers east or west of x = 0 km. Moreover, the recovered amplitudes in all sections rarely exceed 50% of the synthetic input anomalies, indicating that although the lateral variations in S wave velocity immediately beneath the inner floor are likely real, their amplitudes are probably underestimated. For this reason, a three-dimensional V_P/V_S image is likely to be unreliable.

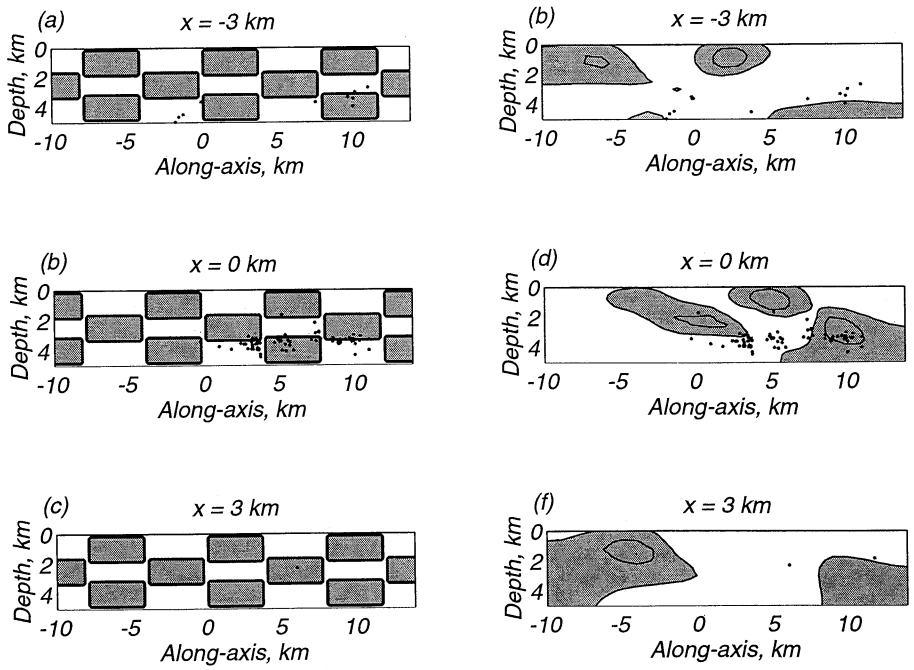

Figure 9. Resolution tests for V_S. Vertical, axis-parallel slices through synthetic and recovered V_S models are shown (a and b) for x = -3 km, (c and d) x = 0 km, and (e and f) x = 3 km. In the recovered model (Figures 9b, 9d, and 9f) the contour interval is 0.1 km/s, and regions with velocity perturbations less than -0.2 km/s are shaded; the shaded regions in the synthetic model represent velocity perturbations of -0.4 km/s. The small solid circles are the hypocenters of the 91 segment center earthquakes, projected onto the nearest vertical plane.

We tested starting V_P/V_S ratios that ranged from 1.7 to 2.1, perturbed the starting hypocentral parameters by up to 1 km in the x, y, and z directions and up to 1 s in origin time, tested different starting P wave velocity models (a one-dimensional model derived from *Hooft et al.* [2000] and a three-dimensional model from *Barclay et al.* [1998]), and explored the effects of tightening and loosening the constraints by varying the multipliers λ_i in (3). For all of the models with acceptable RMS residual values we obtained similar hypocenters (with a maximum vector difference of a few hundred meters) and velocity models. The high stability of the method is probably due to the large number of airgun arrivals, which tightly constrain the P wave velocity structure, and starting hypocenters (from the grid search) that were close to the inversion solutions.

The hypocenters determined by joint inversion (Figure 10) have moved little from the grid search solutions except for clustering together more and defining more clearly a linear trend in the along-axis direction when compared with the grid search hypocenters in Figure 4. Although some of this difference may be attributed to the removal of the requirement that hypocenters lie on one of the grid nodes, the maximum possible shift due to this effect for the 250-m grid we used is ~200 m, which is smaller than the average shift of ~500 m. Therefore the more detailed velocity structures used in the joint inversion were also responsible for the change in epicentral distribution. The increased clustering of otherwise independent earthquakes and the reduction in RMS earthquake arrival time residuals indicate that joint inversion gives an improved fit over the grid search results.

4. Source Mechanisms

Earthquake focal mechanisms can be used to infer the nature of the stress field and to address the cause of the seismicity. From the first-motion polarities of the P wave arrivals we were able to determine focal mechanisms for only five segment center earthquakes. Unambiguous mechanisms for the remaining earthquakes could not be determined owing to insufficient coverage of the focal sphere. In addition, the apparent variability of the five mechanisms, even between earthquakes within a single cluster, precluded the use of composite focal mechanisms. Therefore we increased the number of estimated focal mechanisms by supplementing the P wave polarity observations with P/S amplitude ratios.

4.1. Method

We based our method on that of *Shen et al.* [1997]. By this approach the ratio of the first arriving P and S wave amplitudes and the P wave first-motion polarity at all receivers for a given earthquake are inverted using a three-dimensional grid search algorithm for the strike, dip, and slip of the best fitting focal mechanism. For each P and S wave amplitude observation the maximum peak-to-peak amplitude within two cycles of the arrival time pick is used, where the maximum S wave amplitude is measured from the Euclidian norm of the two horizontal components. For the strike, dip, and slip corresponding to each point on the search grid, amplitude ratios and polarities are calculated, assuming a double-couple, point source model [*Herrmann*, 1975]. Takeoff angles and azimuths of rays leaving the source are

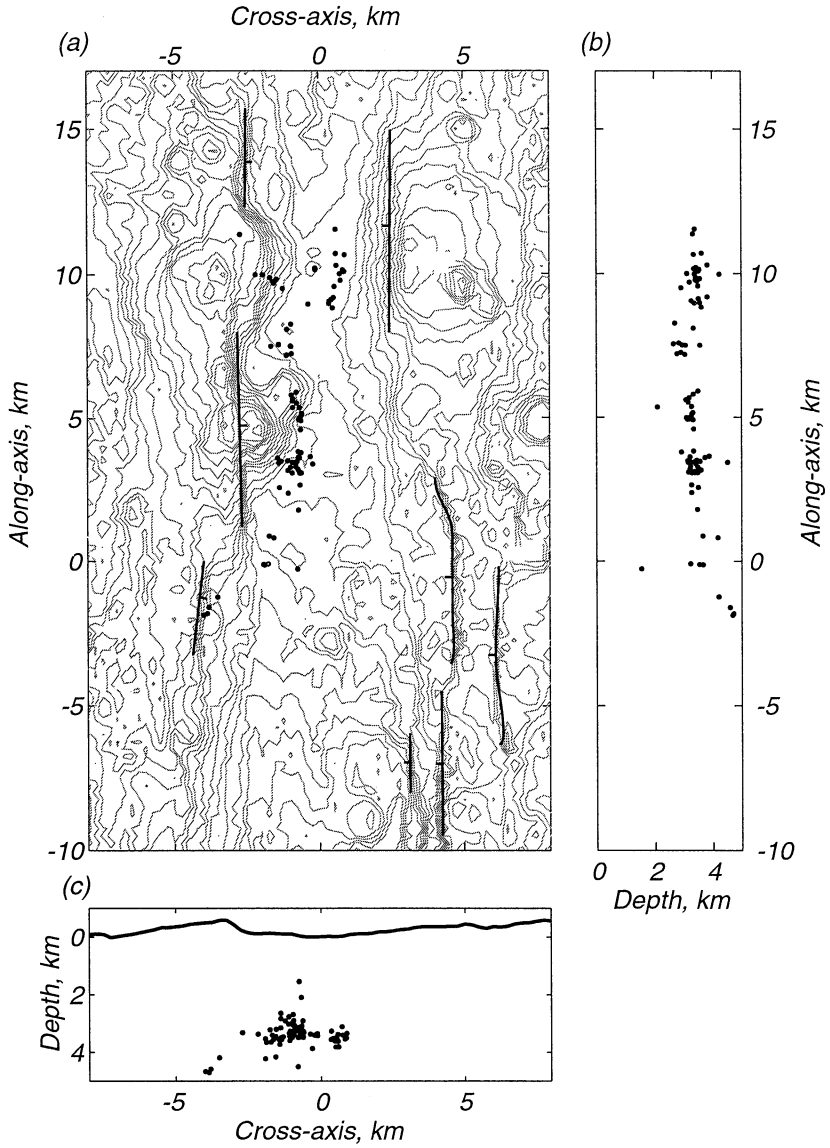

Figure 10. Hypocentral distribution after joint inversion for locations and structure. (a) Epicenters after joint inversion, plotted on bathymetry; 50-m contour interval. Positions of the major scarps are outlined. (b) Focal depths projected onto an axis-parallel vertical plane. (c) Focal depths projected onto an axis-perpendicular vertical plane. The solid line is a cross-axis bathymetric profile, located at $y = 7$ km in Figure 10a. The coordinate system is the same as for Figure 4.

required; we determined these angles from the results of the ray tracing in section 3.3.

The misfit function we used in the grid search is

$$\frac{\sum_{i=1}^{N} w_i \left[\ln\left(r_i \frac{S_i}{P_i} \right) \right]^2}{\sum_{i=1}^{N} w_i} + \lambda \sum_{j=1}^{L} P_j , \qquad (4)$$

where for the ith OBS, r_i is the observed, corrected P/S amplitude ratio (see below); S_i and P_i are the predicted S and P wave amplitudes, respectively, for a particular focal mechanism; w_i is the instrument weighting factor; and N is the number of OBSs. The second term in (4), the polarity misfit, is the sum of the predicted P wave amplitudes P_j for the L OBSs for which the predicted and observed P wave polarities did not match. The multiplier λ is used to control the relative importance of the polarity constraints.

The misfit function (4) differs from (6) of *Shen et al.* [1997] in the treatment of polarity constraints. Instead of rejecting models with one or more mismatched P wave polarities, we increased their misfit. This modification was motivated by the observation that many models were rejected on the basis of a single polarity mismatch near P wave amplitude nodal lines. However, our estimated uncertainty in the takeoff angle and azimuth of an arrival was 5°-10°, large enough to place near-nodal polarity observations in the wrong quadrant. By adding the P wave amplitude for each mismatched polarity observation to the misfit function we decreased the importance of the polarity constraints for points

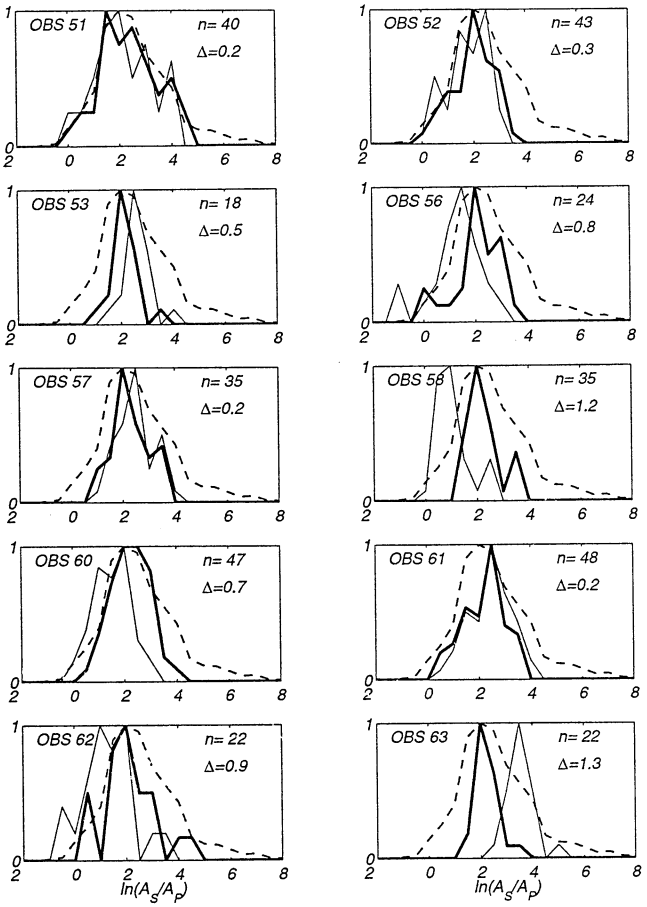

Figure 11. Determination of near-surface correction factor for *S/P* amplitude applied to each OBS. Each plot shows the normalized distribution of *S/P* amplitude ratios. The dashed line represents the distribution expected for a random set of 1000 focal mechanisms, the thin solid line shows the observed distribution for n observations at each OBS, and the thick solid line is the observed distribution after multiplication by the correction factor, e^{Δ}.

close to the nodal planes. The relative contribution of polarity constraints to the misfit was controlled by the constant λ, where $\lambda=0$ removes the polarity constraints and $\lambda=\infty$ corresponds to the approach of *Shen et al.* [1997]. From inspection of a sample of rejected models we chose $\lambda=10$.

The observed amplitude ratios were corrected for different near-surface and instrument amplifications of P and S waves, following the approach of *Shen et al.* [1997]. The amplitude ratios at each receiver were corrected by a constant multiplier in order to match the amplitude ratio distribution for a random set of focal mechanisms. Observed and random distributions for 10 OBSs from our experiment are shown in Figure 11. The multiplicative correction factors ranged from 0.25 to 3.3. An important assumption of this approach is that the observed amplitude ratio distribution at each receiver is random. In our case, we expect that each OBS samples a near-random distribution of amplitude ratios since the azimuths and source-receiver ranges are variable. This assumption can be tested by comparing the widths of the observed and random amplitude ratio distributions. In our case (Figure 11), the observed distributions are narrower than the random ones. This is expected because amplitude ratios near the tails of the observed distribution would be due to very small P or S amplitudes, which would not be picked and would therefore be underrepresented in the distribution. We assumed that this effect truncated both tails of each amplitude ratio distribution to a similar degree, and we therefore concluded that the correction was valid for most instruments. Two OBSs (OBS 53 and OBS 63 in Figure 11), however, had significantly narrower distributions, and we down weighted by 50% the importance of these instruments in the grid search.

In order to confirm that the corrections made a noticeable improvement we perturbed the correction factors, searched for the best fitting mechanisms for 43 well-constrained earthquakes, and averaged their misfits. The perturbation tests included multiplying all correction factors by a constant amount, multiplying individual factors by random amounts between $1/e$ and e, and removing the corrections altogether. The results (Figure 12) show that for all perturbations the unperturbed set of corrections gave the minimum average misfit, and we conclude that the corrections do indeed make an improvement to the solutions.

We restricted our analysis to well-recorded earthquakes with epicenters that were within or close to the OBS network, including the five events with mechanisms determined from P wave polarities. Of these, we only considered overdetermined mechanisms (those with four or more amplitude ratio observations), and since amplitude ratio information alone cannot constrain the polarity of a focal mechanism, earthquakes with no P wave polarity observations were rejected. We then applied the grid search inversion to the 43 remaining earthquakes, removed the most poorly fit amplitude ratio observations, and repeated the grid search. For each

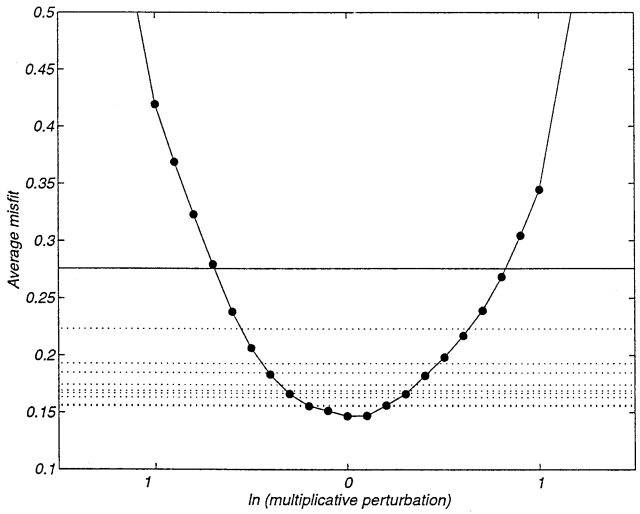

Figure 12. Average misfit of the best fitting mechanism models for 43 microearthquakes, under a variety of perturbations applied to the correction factors of Figure 11. Horizontal solid line is the average misfit with no correction. Each circle represents the average misfit obtained for a single multiplicative perturbation applied to the correction factors for all OBSs. Each dotted line represents the average misfit after multiplying each of the OBS correction factors by a random value between e^{-1} and e. All of these perturbation tests gave average misfits that were larger than the unperturbed correction factor.

solution we determined an approximate 95% confidence parameter subspace on the basis of an F test, and we rejected an additional 11 earthquakes for which one or more of the model parameters were poorly constrained.

4.2. Results

Focal mechanisms for the 32 earthquakes are shown in Figure 13. Twenty-five mechanisms (~80%) are consistent with normal faulting on steeply dipping planes that strike within 30° of the trend of the axial valley. Nearly half of these focal mechanisms indicate slip on near-vertical or horizontal planes, but given the uncertainties in the *P/S* amplitude ratio method, the dips of these mechanisms may be shallower, and we consider them to be consistent with high-angle normal faulting. The remaining nine have large strike-slip components or have planes striking >30° from the axial valley trend. These nine mechanisms were as well constrained as the others since their 95% confidence regions were not noticeably larger. Seven of these mechanisms are located within the large epicentral cluster near (x = -1, y = 3).

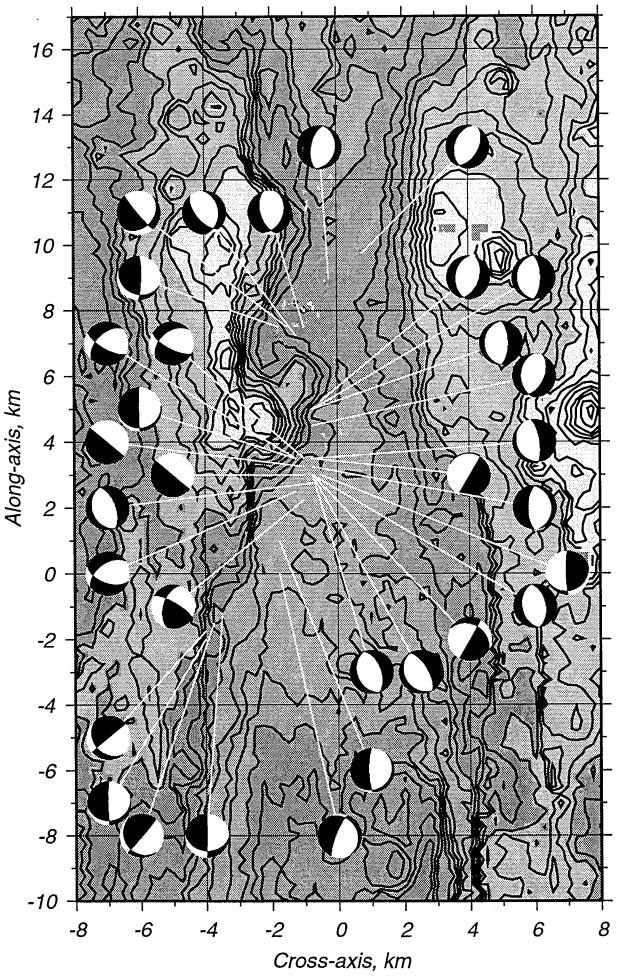

Figure 13. Focal mechanisms for 32 segment center earthquakes, superimposed on bathymetry; 50-m contour interval. Mechanisms that best fit the *P/S* amplitude ratios and *P* wave polarities are shown for each earthquake; equal-area projections are of the lower focal hemisphere; compressional quadrants are shaded. White lines point to the epicenters. The coordinate system is the same as for Figure 4.

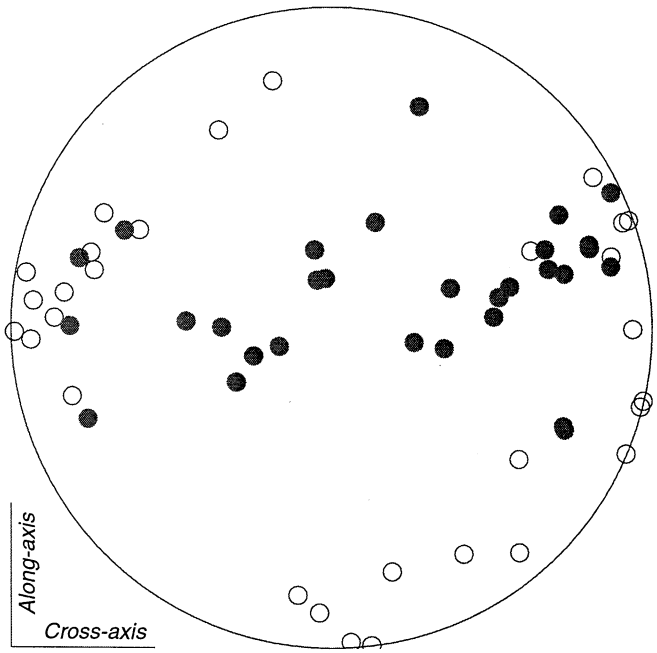

Figure 14. P and T axes for the focal mechanisms (determined from amplitude ratios) in Figure 13, plotted on an equal-area projection of the lower focal hemisphere. Solid circles represent P (compressional) axes, and open circles represent T (tensional) axes.

A plot of the *P* and *T* axes (Figure 14) shows a belt of *P* axes plunging at a well-distributed range in angles in the cross-axis direction; *T* axes are mainly horizontal, and two thirds also lie in the cross-axis direction.

We tested the null hypothesis that the observed focal mechanisms can be explained by a single stress field consistent with plate spreading (greatest compressive principal stress σ_1 vertical and least compressive principal stress σ_3 horizontal and parallel to the spreading direction). Since the direction of slip on a fault depends on both the fault orientation and the stress field, the variability in focal mechanisms in Figure 13 may be due to heterogeneities in the stress field or faulting on differently oriented planes of weakness under a single stress field. We applied the method of *Gephart and Forsyth* [1984] to determine if the observed focal mechanisms were consistent with a single, plate-spreading model of stress by finding the minimum rotation of each focal mechanism solution that was required to make it consistent with such a stress field. By this approach the directions of σ_1 and σ_3 were fixed, while the parameter $R = (\sigma_1-\sigma_2)/(\sigma_1-\sigma_3)$ [*Gephart and Forsyth,* 1984], where σ_2 is the intermediate principal stress, was allowed to vary. We considered that a rotation of <20° indicates a consistent stress field and focal mechanism, following *Gephart and Forsyth* [1984]. Of the 32 earthquakes, 25 required rotations of <20° to fit the stress model. From this result we conclude that most (80%) of the focal mechanisms are consistent with a single axis-perpendicular extensional stress field. The best fitting value of R was 0.9, which suggests that at 3-4 km depth, $|\sigma_2|$ and $|\sigma_3|$ are comparable. Another indication that $|\sigma_2|$ and $|\sigma_3|$ are comparable in the vicinity of the earthquakes is the large azimuthal range of *T* axes (Figure 14).

We have assumed that all of the earthquakes in Figure 13 have double-couple source mechanisms. However, microearthquakes with non-double-couple mechanisms are common in volcanic and geothermal areas [e.g., *Miller et al.*, 1998]. Because earthquakes having a significant non-double-couple component cannot be identified from our data, we cannot rule out their occurrence at the 35°N segment center. If such events were present, the *P/S* amplitude ratio method would give erroneous results. However, because we can explain most (80%) of the focal mechanisms in Figure 13 as shear failure in response to the expected extensional stress field, we infer that most or all of the mechanisms are predominantly double couple in nature. The remaining 20% of the focal mechanisms may be due to shear failure in a spatially heterogeneous stress field.

5. Other Source Parameters

We also estimated seismic moments and other source parameters for 114 segment center earthquakes from the far-field displacement spectra [*Brune*, 1970; *Hanks and Wyss*, 1972], following the approach of *Toomey et al.* [1988] and *Kong et al.* [1992]. The moments (obtained from spectra of the *P* and *S* arrivals for each earthquake) ranged from 5 x 10^{16} to 2x10^{19} dyn cm (1 dyn cm = 10^{-7} N m). These values are comparable to but generally smaller than the moments calculated at other sites on the MAR [*Toomey et al.*, 1988; *Kong et al.*, 1992; *Wolfe et al.*, 1995]. Other parameters estimated were source dimension (70-130 m), stress drop (0.03-4 MPa), and fault displacement (0.05-7 mm).

Earthquake clusters typically have a size-frequency power law distribution of the form $N(M_0) = aM_0^{-b}$, where N is the number of earthquakes with moment $\geq M_0$ [e.g., *Scholz*, 1990]. Higher values of b indicate a larger proportion of smaller earthquakes and are a characteristic of magmatically active regions where b (corrected for M_0 instead of M_L) often exceeds the global average of 0.7 by a factor of 2 [e.g., *Wyss et al.*, 1997]. At the 35°N segment center we find a b value of 0.94 ± 0.05 (Figure 15). At the segment near 26°N on the MAR, *Kong et al.* [1992] found higher b values (1.1-1.5) near the segment center than at the segment ends (0.6-0.9) and inferred a larger magmatic signature at the segment center. *Wolfe et al.* [1995] determined a value of 0.8 for the segment at 29°N, while at 23°N, *Toomey et al.* [1988] measured values of 0.5 in the off-axis rift mountains and 0.8 in the inner valley. The value we measure is near the center of this range of values and within the typical range for volcanic areas.

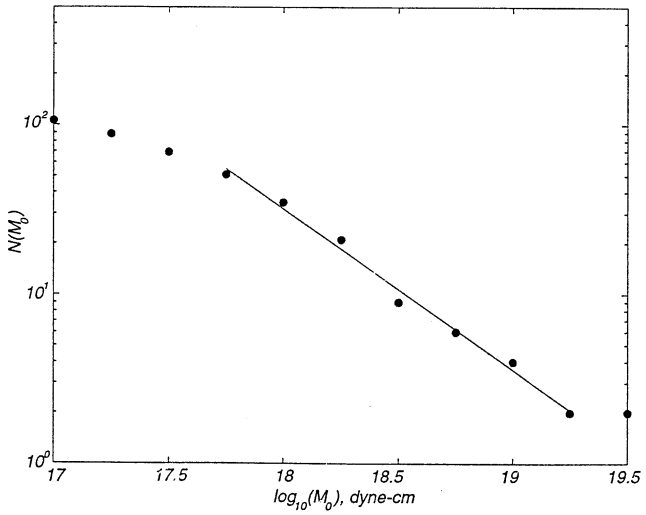

Figure 15. Distribution of seismic moments. Each point denotes the number of earthquakes $N(M_0)$ with moment greater than M_0. The b value is the slope of the best fitting line (solid line) such that $\log_{10}[N(M_0)] = a\text{-}bM_0$.

6. Interpretation

6.1. Tectonic Setting of Microearthquakes

The microearthquake activity observed at the ends of the segment is concentrated near the inside corners (Figure 1). Although these epicenters are poorly constrained owing to the uncertainty in V_P/V_S structure, they concentrated near the inside corners for a wide range (1.7-2.0) in assumed mean V_P/V_S values. The morphology of inside corners has been primarily attributed to deformation and faulting [e.g., *Tucholke and Lin,* 1994], and the segment end epicentral distributions at 35°N are consistent with this interpretation.

From the spatial relationships between the hypocenters at the segment center and the scarps that define the walls of the inner valley, we suggest that the earthquakes are associated with valley-bounding normal faults. The western wall of the inner valley is defined by a series of eastward dipping scarps (Figure 4a) from y = -4 to y = 15. A single active fault scarp may run along x = -2 from y = 0 to y = 15, although it is unclear from the multibeam bathymetry data alone whether it steps inward between y = 8 and y = 12 km. We interpret the feature centered at x = -2, y = 5 to be a near-axis seamount [*Barclay et al.*, 1998], and therefore the scarp between y = 8 and y = 12 km may also be volcanic in origin. That the main scarp and the seismicity are both situated between y = 0 km and y = 15 km supports an association between the two. In addition, a plane that intersects the base of the main scarp and passes through the cluster of segment center hypocenters has an eastward dip of ~60° (Figure 10c), which is the expected dip of a normal fault initiated in an extensional regime, according to Mohr-Coulomb theory [*Thatcher and Hill,* 1995]. With this interpretation, however, the cluster of seismicity at x = 1, y = 10 cannot be associated with the same fault plane. We suggest that this cluster may lie on a second fault: a westward dipping (~70°) fault that forms the eastern wall of the inner valley, an eastward dipping fault associated with the inward step of the western wall between y = 8 and y = 12 km, or a secondary branch of the main western valley-bounding fault. An alternative explanation is that the western valley-bounding fault soles into a ductile detachment beneath the inner valley and that the easternmost cluster lies on a subhorizontal continuation of the fault plane. However, slip on a subhorizontal plane is not supported by the single fault plane solution we obtained from this cluster (Figure 13), which shows nodal planes dipping at ~45°.

That the maximum earthquake depth is nearly constant at 4 km along a 12-km length of the inner valley suggests that this feature is characteristic of the segment center, an inference made despite the relatively short duration (43 days) of the experiment on which the observation is based. We interpret this feature to be the base of the seismogenic layer. Additional support for this interpretation is provided by the observation that most of the earthquakes lie between 3- and 4-

km depth. For brittle failure or frictional sliding the stress energy increases with depth [*Sibson,* 1982], and a maximum in seismicity is often observed just above the base of the inferred seismogenic zone [*Meissner and Strehlau,* 1982; *Sibson,* 1982, 1984].

The segment center seismicity is plausibly attributable to brittle deformation in regions of stress concentration near the toe of one or two normal faults. The spatial association with the faults, the concentration of seismicity near the inferred base of the seismogenic layer, and the strong grouping of the hypocenters are all consistent with failure at asperities or other loci of increased stresses at 3-4-km depth. In addition, most (23 out of 32) of the focal mechanisms show normal faulting along faults striking approximately parallel to the ridge axis, and 25 out of 32 are consistent with horizontal extension in the cross-axis direction. An alternative explanation for the seismicity is localized differential thermal contraction and failure, which has been invoked for segment center microearthquakes at 26°N [*Kong et al.*, 1992] and 29°N [*Wolfe et al.*, 1995] on the MAR. This second explanation may be particularly appropriate for the center of the 35°N segment because the seismicity there is restricted to a region that also has a strong magmatic signature [*Barclay et al.,* 1998]. For most of the microearthquakes, however, we prefer the former explanation, on the basis of the predominantly normal faulting mechanisms. Seismicity caused by differential thermal contraction and cracking is generally identified by heterogeneous or anomalous source mechanisms [*Miller et al.,* 1998], however, and may be responsible for the mechanisms that are not consistent with normal faulting.

6.2. Interpretation of *P* and *S* Wave Velocity structures

As discussed by *Barclay et al.* [1998], the lateral variations in *P* wave velocity (Figure 7) may be attributed either to variations in temperature and melt fraction or to variations in porosity. The spatial association between the pronounced low-velocity volume and the near-axis seamount is consistent with a shallow body at near-solidus temperatures. With this interpretation the along-axis low-velocity band at 2-3 km depth in Figure 7 may represent elevated temperatures, and the displacement of the band toward the western half of the inner valley floor may reflect increased or most recent magmatism there. An alternative explanation is that the low-velocity band is caused by increased fracturing and porosity in the vicinity of the inferred plane of the western valley-bounding fault. The decreased *S* wave velocities beneath the western half of the inner valley (Figure 7) are also consistent with an increase in crack porosity or higher temperatures [*Christensen,* 1996]. Our preferred interpretation of the depth-dependent V_P/V_S results, discussed below, requires the presence of cracks to 2.5-km depth and is thus consistent with a porosity-based interpretation.

We attribute the depth variations in the V_P/V_S ratio (Figure 6) to varying crack abundances and aspect ratios. As the V_P/V_S value for an uncracked, unaltered basalt or gabbro is 1.8-1.9 [*Hyndman,* 1979; *Johnston and Christensen,* 1997], an additional mechanism is required to explain our results. High V_P/V_S values (of 2.5 or more) in seismic layer 2A have been observed elsewhere and have been attributed to a high crack porosity [e.g., *Hyndman,* 1979; *Collier and Singh,* 1998]. We interpret the decrease in V_P/V_S at 1-2-km depth as a decrease in the proportion of thin cracks compared to thick cracks. This interpretation has been invoked to explain the low V_P/V_S values at similar depths in young oceanic crust elsewhere [*Shearer,* 1988; *Shaw,* 1994]. Possible causes for a decreasing thin-crack porosity with depth are preferential crack closure by increasing confining pressure [*Nur and Simmons,* 1970] and sealing of cracks with hydrothermal minerals [*Wilkens et al.,* 1991].

7. Discussion

The base of the seismogenic layer beneath the segment center at 35°N, at 4-km depth, is shallower than at other MAR segments at which microearthquake experiments have been conducted. The maximum microearthquake depth is 7 km at 29°N [*Wolfe et al.,* 1995], 6 km at 26°N [*Kong et al.*, 1992], and 8 km at 23°N [*Toomey et al.,* 1988]. We suggest that the shallower seismicity at 35°N may be due to crustal temperatures that are higher at a given depth than at the other three segments. The limit to seismicity at the base of the seismogenic zone is thought to be due to the transition from unstable, velocity-weakening friction to stable, velocity-strengthening friction [*Tse and Rice*, 1986], a transition that occurs close to but shallower than the brittle-plastic transition for bulk deformation [*Scholz,* 1988]. In addition to temperature this transition is influenced by strain rate, rock composition, and the presence of water [e.g., *Hirth et al.,* 1998]. However, under the assumption that these effects are similar for all four MAR segments a relative increase in temperature is the most likely reason for the thinner seismogenic layer at 35°N. This suggestion is consistent with the enhanced crustal magmatism at the 35°N segment center.

The variation in maximum focal depth, interpreted as the depth to the base of the seismogenic zone beneath the inner valley for the four MAR segments correlates with the variation in cross-axis relief, as shown in Figure 16a. This relationship is consistent with a thicker, colder lithosphere below regions of greater inner valley relief, in qualitative agreement with lithospheric stretching models for axial topographic relief at slow spreading ridges [e.g., *Shaw,* 1992; *Shaw and Lin,* 1996; *Poliakov and Buck,* 1998]. The maximum depth of seismicity, however, cannot be directly compared to the depth of a sharp brittle-ductile transition commonly assumed in modeling studies owing to the likely nonzero thickness of a zone of aseismic, semibrittle deformation beneath the seismogenic zone that contributes significantly to the strength of the lithosphere [e.g., *Scholz,* 1988]. In addition, the relationship between cross-axis relief and maximum depth of seismicity is probably more complicated than that suggested by Figure 16a. For example, simple thermomechanical stretching models cannot explain the asymmetry in the shape of the inner valley at segment ends, where the extensional stresses are influenced by ridge offsets and spreading is accommodated by low-angle faulting [e.g., *Escartín and Lin,* 1995].

Cross-axis relief and mantle Bouguer anomaly (MBA) also correlate for the four MAR segments. The relative MBA, defined as the difference in along-axis MBA between the location of the microearthquakes and the end of the segment, is plotted versus cross-axis relief in Figure 16b; the relative MBA for segment end seismicity (at 23°N and 29°N) is set to 0. Under the assumption that the crustal thickness at the ends

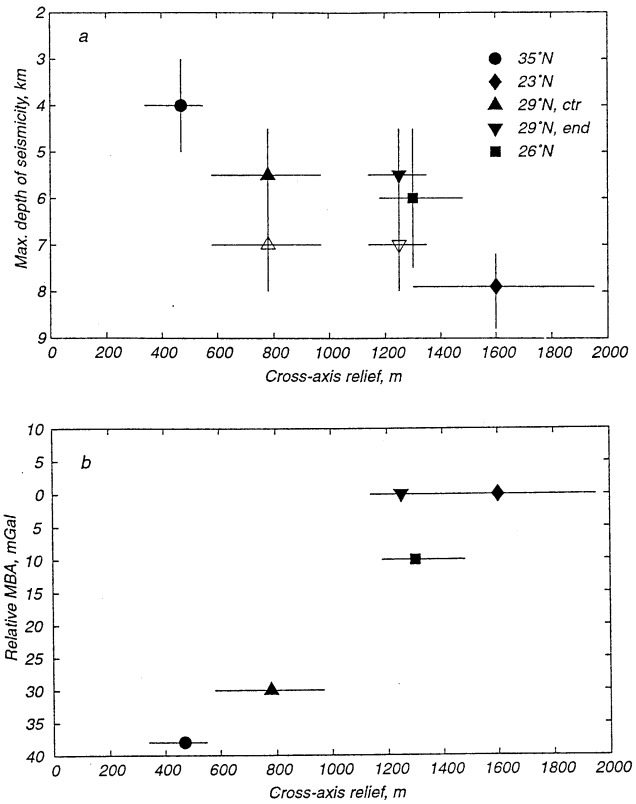

Figure 16. Relation between cross-axis relief, maximum depth of seismicity, and mantle Bouguer anomaly (MBA) variation for four MAR segments. (a) Maximum depth of seismicity and cross-axis relief. The maximum depth of seismicity was estimated from the focal depths of inner valley microearthquakes from 23°N [*Toomey et al.*, 1985], 26°N [*Kong et al.*, 1992], 29°N [*Wolfe et al.*, 1995], and 35°N (this study). The cross-axis relief was determined by averaging the relief from the inner valley floor to the first crest of the valley walls for a series of cross-axis bathymetric profiles in the vicinity of the earthquake epicenters. Error bars on relief span the maximum and minimum relief of all the profiles in each series. Error bars on the maximum earthquake depths were taken from the reported 95% errors for the deepest earthquakes in each study. Data from 29°N are divided into segment center and segment end earthquakes and by whether hypocenters were determined using arrivals from only four OBSs (open symbols) or from five or more OBSs (solid symbols). (b) Relative mantle Bouguer anomaly and cross-axis relief. Data are plotted for the same four segments: 23°N [*Morris and Detrick*, 1991], 26°N [*Tucholke et al.*, 1997], 29°N [*Lin and Phipps Morgan*, 1992], and 35°N [*Detrick et al.*, 1995]. See text for details.

of each of the four segments is comparable the relative MBA is a proxy for crustal thickness in that more negative values of relative MBA represent thicker crust at the segment center. By comparison with seismic determinations of crustal thickness at two of the locations in Figure 16b (35°N [*Hooft et al.*, 2000] and 23°N [*Purdy and Detrick*, 1986]), a relative MBA value of 0 mGal represents a crustal thickness of ~6 km while a value of -40 mGal corresponds to a crustal thickness of ~8.5 km.

The variations in Figure 16 may reflect differences in the magmatic flux to, and thermal structure of, the four segments. These differences may be due to magmatic episodicity or steady state, along-axis variations in magma supply. The temperature structure of a segment is thought to be a balance between the heat provided by crystallization of the crust, heat flow from the mantle, and hydrothermal cooling of the brittle crust. During a magmatic episode, the crust is thickened and crustal temperatures are increased, thereby elevating the brittle-ductile transition. During an amagmatic period, in contrast, heat flux is reduced, and the maximum depths of hydrothermal circulation and seismicity likely increase. This episodicity may simply modulate steady state variations in thermal structure, such as those between the ends and center of an individual segment.

8. Conclusions

1. Microearthquake seismicity on the MAR near 35°N during a 43-day period was concentrated at the ends and center of the segment. The segment end seismicity occurred predominantly at the inside ridge offset corners.

2. The segment center seismicity is strongly clustered, is spatially related to axis-parallel fault scarps that bound the inner valley, and is characterized by predominantly normal faulting mechanisms. We interpret these earthquakes as the result of stress concentrations near the toes of valley-bounding normal faults, at the base of the seismogenic layer.

3. The horizontally averaged V_P/V_S ratio at the segment center decreases from 2.9 in seismic layer 2A to 1.7 at 2 km depth. We attribute this decrease to a decreasing contribution of thin cracks to fracture porosity with depth, the result of preferential closing or sealing.

4. The depth to the base of the inferred seismogenic zone at the segment center is ~4 km, anomalously shallow compared with other MAR segments. We attribute this shallower maximum focal depth to higher lithospheric temperatures at 35°N than at other segments at which microearthquake experiments have been carried out. There is a positive correlation between cross-axis relief and maximum earthquake depth for four MAR segments.

Acknowledgments. We thank the Woods Hole Oceanographic Institution OBS group and the captains and crews of the R/V *Ewing* and the R/V *Oceanus*. We are grateful to John Gephart, Yang Shen, and Cecily Wolfe for providing their software for stress inversion, focal mechanism grid search, and moment magnitude, respectively, and to John Collins, Rob Dunn, and Laura Magde for discussions. Mary Fowler, Satish Singh, and an anonymous reviewer provided helpful comments. This work was supported by the National Science Foundation under grants OCE-9018389 and OCE-9530146.

References

Au, D., and R. M. Clowes, Shear-wave velocity structure of the oceanic lithosphere from ocean bottom seismometer studies, *Geophys. J. R. Astron. Soc., 77*, 105-123, 1984.

Barclay, A. H., D. R. Toomey, G. M. Purdy, and S. C. Solomon, Crustal anisotropy and tomographic imaging of V_P/V_S structure beneath the axial high of a slow spreading ridge segment (abstract), *Eos Trans. AGU, 76* (46), Fall Meet. Suppl., F609, 1995.

Barclay, A. H., D. R. Toomey, and S. C. Solomon, Seismic structure and crustal magmatism at the Mid-Atlantic Ridge, 35°N, *J. Geophys. Res., 103*, 17,827-17,844, 1998.

Bideau, D., R. Hekinian, C. Bollinger, M. Constantin, E. Gracia, C. Guivel, B. Sichler, R. Apprioul, and R. Le Gall, Submersible investigation of highly contrasted magmatic activities recorded on

two segments of the Mid-Atlantic Ridge near 34°52'N and 33°55'N, *InterRidge News, 5*, 9-14, 1996.

Brune, J. N., Tectonic stress and the spectra of seismic shear waves from earthquakes, *J. Geophys. Res., 75,* 4997-5009, 1970. (Correction, *J. Geophys. Res., 76,* 5002, 1971.)

Chen, Y., and W. J. Morgan, Rift valley/no rift valley transition at mid-ocean ridges, *J. Geophys. Res., 95,* 17,571-17,581, 1990.

Christensen, N. I., Poisson's ratio and crustal seismology, *J. Geophys. Res., 101,* 3139-3156, 1996.

Christeson, G. L., P. R. Shaw, and J. D. Garmany, Shear and compressional wave structure of the East Pacific Rise, *J. Geophys. Res., 102,* 7821-7835, 1997.

Collier, J. S., and S. C. Singh, Poisson's ratio structure of young oceanic crust, *J. Geophys. Res., 103,* 20,981-20,996, 1998.

Detrick, R. S., H. D. Needham, and V. Renard, Gravity anomalies and crustal thickness variations along the Mid-Atlantic Ridge between 33°N and 40°N, *J. Geophys. Res., 100,* 3767-3787, 1995.

Escartín, J., and J. Lin, Ridge offsets, normal faulting, and gravity anomalies of slow spreading ridges, *J. Geophys. Res., 100,* 6163-6177, 1995.

Francis, T. J. G., The ratio of compressional to shear velocity and rock porosity on the axis of the Mid-Atlantic Ridge, *J. Geophys. Res., 81,* 4361-4364, 1976.

Gephart, J. W., and D. W. Forsyth, An improved method for determining the regional stress tensor using earthquake focal mechanism data: Application to the San Fernando earthquake sequence, *J. Geophys. Res., 89,* 9305-9320, 1984.

Hanks, T. C., and M. Wyss, The use of body-wave spectra in the determination of seismic-source parameters, *Bull. Seismol. Soc. Am., 62,* 561-589, 1972.

Herrmann, R. B., A student's guide to the use of *P* and *S* wave data for focal mechanisms determination, *Earthquake Notes, 46*, 29-39, 1975.

Hirth, G., J. Escartín, and J. Lin, The rheology of the lower oceanic crust: Implications for lithospheric deformation at mid-ocean ridges, in *Faulting and Magmatism at Mid-Ocean Ridges, Geophys. Monogr. Ser.,* vol. 106, edited by W. R. Buck, P. T. Delaney, J. A. Karson, and Y. Lagabrielle, pp. 291-304, AGU, Washington, D.C., 1998.

Hooft, E. E. E., R. S. Detrick, D. R. Toomey, J. A. Collins, and J. Lin, Crustal thickness and structure along three contrasting spreading segments of the Mid-Atlantic Ridge, 33.5°-35°N, *J. Geophys. Res., 105,* 8205-8226, 2000.

Hussenoeder, S. A., Seismic and magnetic constraints on the structure of upper oceanic crust at fast and slow spreading ridges, Ph. D. thesis, Woods Hole Oceanogr. Inst./Mass. Inst. of Technol. Joint Program, Woods Hole, 1998.

Hyndman, R. D., Poisson's ratio in the oceanic crust -- A review, *Tectonophysics, 59,* 321-333, 1979.

Johnston, J. E., and N. I. Christensen, Seismic properties of layer 2 basalts, *Geophys. J. Int., 128,* 285-300, 1997.

Klein, F. W., Hypocenter location program HYPOINVERSE, 1, User's guide to versions 1, 2, 3, 4, *U.S. Geol. Surv. Open File Rep., 78-694,* 103 pp., 1978.

Kong, L. S. L., S. C. Solomon, and G. M. Purdy, Microearthquake characteristics of a mid-ocean ridge along-axis high, *J. Geophys. Res., 97,* 1659-1685, 1992.

Lin, J., and J. Phipps Morgan, The spreading rate dependence of three-dimensional mid-ocean ridge gravity structure, *Geophys. Res. Lett., 19*, 13-16, 1992.

Lin, J., G. M. Purdy, H. Schouten, J.-C. Sempere, and C. Zervas, Evidence from gravity data for focused magmatic accretion along the Mid-Atlantic Ridge, *Nature, 344*, 627-632, 1990.

Magde, L. S., A. H. Barclay, D. R. Toomey, R. S. Detrick, and J. A. Collins, Crustal magma plumbing within a segment of the Mid-Atlantic Ridge, 35°N, *Earth Planet. Sci. Lett., 175*, 55-67, 2000.

Meissner, R., and J. Strehlau, Limits of stresses in continental crusts and their relation to the depth-frequency distribution of shallow earthquakes, *Tectonics, 1*, 73-89, 1982.

Michelini, A., Testing the reliability of V_P/V_S anomalies in traveltime tomography, *Geophys. J. Int., 114,* 405-410, 1993.

Miller, A. D., G. R. Foulger, and B. R. Julian, Non-double-couple earthquakes; 2, Observations, *Rev. Geophys., 36,* 551-568. 1998.

Morris, E., and R. S. Detrick, Three-dimensional analysis of gravity anomalies in the MARK area, Mid-Atlantic Ridge 23°N, *J. Geophys. Res., 96,* 4355-4366, 1991.

Moser, T. J., Shortest path calculation of seismic rays, *Geophysics, 56,* 59-67, 1991.

Nur, A., and G. Simmons, The origin of small cracks in igneous rocks, *Int. J. Rock Mech. Min. Sci., 7*, 307-314, 1970.

Phipps Morgan, J., E. M. Parmentier, and J. Lin, Mechanisms for the origin of mid-ocean ridge axial topography: Implications for the thermal and mechanical structure of accreting plate boundaries, *J. Geophys. Res., 92,* 12,823-12,836, 1987.

Poliakov, A. N. B., and W. R. Buck, Mechanics of stretching elastic-plastic-viscous layers: Applications to slow-spreading mid-ocean ridges, in *Faulting and Magmatism at Mid-Ocean Ridges, Geophys. Monogr. Ser.,* vol. 106, edited by W. R. Buck, P. T. Delaney, J. A. Karson, and Y. Lagabrielle, pp. 291-304, AGU, Washington, D.C., 1998.

Purdy, G. M., and R. S. Detrick, Crustal structure of the Mid-Atlantic Ridge at 23°N from seismic refraction studies, *J. Geophys. Res., 91,* 3739-3762, 1986.

Rowlett, H., and D. W. Forsyth, Recent faulting and microearthquakes at the intersection of the Vema Fracture Zone and the Mid-Atlantic Ridge, *J. Geophys. Res., 89,* 6079-6094, 1984.

Scholz, C. H., The brittle-plastic transition and the depth of seismic faulting, *Geol. Rundsch., 77,* 319-328, 1988.

Scholz, C. H., *The Mechanics of Earthquakes and Faulting*, 439 pp., Cambridge Univ. Press, New York, 1990.

Shaw, P. R., Ridge segmentation, faulting and crustal thickness in the Atlantic Ocean, *Nature, 358,* 490-493, 1992.

Shaw, P. R., Age variations of oceanic crust Poisson's ratio: Inversion and a porosity evolution model, *J. Geophys. Res., 99,* 3057-3066, 1994.

Shaw, W. J., and J. Lin, Models of ocean ridge lithospheric deformation: Dependence on crustal thickness, spreading rate, and segmentation, *J. Geophys. Res., 101*, 17,977-17,993, 1996.

Shearer, P. M., Cracked media, Poisson's ratio and the structure of the upper oceanic crust, *Geophys. J., 92,* 357-362, 1988.

Shen, Y., D. W. Forsyth, J. Conder, and L. M. Dorman, Investigation of microearthquake activity following an intraplate teleseismic swarm on the west flank of the southern East Pacific Rise, *J. Geophys. Res., 102,* 459-475, 1997.

Sibson, R. H., Fault zone models, heat flow, and the depth distribution of earthquakes in the continental crust of the United States, *Bull. Seismol. Soc. Am., 72*, 151-163, 1982.

Sibson, R. H., Roughness at the base of the seismogenic zone: Contributing factors, *J. Geophys. Res., 89*, 5791-5799, 1984.

Sleep, N. H., and B. R. Rosendahl, Topography and tectonics of mid-oceanic ridge axes, *J. Geophys. Res., 84,* 6831-6839, 1979.

Sohn, R. A., J. A. Hildebrand, and S. C. Webb, Postrifting seismicity and a model for the 1993 diking event on the CoAxial segment, Juan de Fuca Ridge, *J. Geophys. Res., 103,* 9867-9877, 1998.

Spudich, P., and J. Orcutt, Petrology and porosity of an oceanic crustal site: Results from wave form modeling of seismic refraction data, *J. Geophys. Res., 85,* 1409-1433, 1980.

Takanami, T., and G. Kitagawa, A new efficient procedure for the estimation of onset times of seismic waves, *J. Phys. Earth, 36*, 267-290, 1988.

Tapponnier, P., and J. Francheteau, Necking of the lithosphere and the mechanics of slowly accreting plate boundaries, *J. Geophys. Res., 83,* 3955-3970, 1978.

Thatcher, W., and D. P. Hill, A simple model for the fault-generated morphology of slow-spreading mid-oceanic ridges, *J. Geophys. Res., 100,* 561-570, 1995.

Tolstoy, M. A., A. J. Harding, and J. A. Orcutt, Crustal thickness on the Mid-Atlantic Ridge: Bull's eye gravity anomalies and focused accretion, *Science, 262,* 726-729, 1993.

Toomey, D. R., S. C. Solomon, G. M. Purdy, and M. H. Murray, Microearthquakes beneath the median valley of the Mid-Atlantic Ridge near 23°N: Hypocenters and focal mechanisms, *J. Geophys. Res., 90,* 5443-5458, 1985.

Toomey, D. R., S. C. Solomon, and G. M. Purdy, Microearthquakes beneath the median valley of the Mid-Atlantic Ridge near 23°N: Tomography and tectonics, *J. Geophys. Res., 93,* 9093-9112, 1988.

Toomey, D. R., S. C. Solomon, and G. M. Purdy, Tomographic

imaging of the shallow crustal structure of the East Pacific Rise at 9°30'N, *J. Geophys. Res., 99,* 24,135-24,157, 1994.

Tse, S. T., and J. R. Rice, Crustal earthquake instability in relation to the depth variation of frictional slip properties, *J. Geophys. Res., 91,* 9452-9472, 1986.

Tucholke, B. E., and J. Lin, A geological model for the structure of ridge segments in slow spreading crust, *J. Geophys. Res., 99,* 11,937-11,958, 1994.

Tucholke, B. E., J. Lin, M. C. Kleinrock, M. A. Tivey, T. B. Reed, J. Goff, and G. E. Jaroslow, Segmentation and crustal structure of the western Mid-Atlantic Ridge flank, 25°25'-27°10'N and 0-29 m.y., *J. Geophys. Res., 102,* 10,203-10,223, 1997.

Wilcock, W. S. D., and D. R. Toomey, Estimating hypocentral uncertainties for marine microearthquake surveys: A comparison of the generalized inverse and grid search methods, *Mar. Geophys. Res., 13,* 161-171, 1991.

Wilkens, R. H., G. J. Fryer, and J. Karsten, Evolution of porosity and seismic structure of upper oceanic crust: Importance of aspect ratios, *J. Geophys. Res., 96,* 17,981-17,995, 1991.

Wolfe, C. J., G. M. Purdy, D. R. Toomey, and S. C. Solomon, Microearthquake characteristics and crustal velocity structure at 29°N on the Mid-Atlantic Ridge: The architecture of a slow spreading segment, *J. Geophys. Res., 100,* 24,449-24,472, 1995.

Wyss, M., K. Shimazaki, and S. Wiemer, Mapping active magma chambers by *b* values beneath the off-Ito volcano, Japan, *J. Geophys. Res., 102,* 20,413-20,422, 1997.

A. H. Barclay, Department of Geology and Geophysics, Woods Hole Oceanographic Institution, Woods Hole, MA 02543. (abarclay@whoi.edu)

S. C. Solomon, Department of Terrestrial Magnetism, Carnegie Institution of Washington, 5241 Broad Branch Road, N. W., Washington, DC 20015. (scs@dtm.ciw.edu)

D. R. Toomey, Department of Geological Sciences, University of Oregon, Eugene, OR 97403. (drt@newberry.uoregon.edu)

(Received October 12, 1999; revised June 30, 2000;
accepted October 4, 2000.)